

# Environmental Science Nano

Accepted Manuscript

This article can be cited before page numbers have been issued, to do this please use: J. T. Buchman, E. A. Bennett, C. Wang, A. Abbaspour Tamijani, J. Bennett, B. Hudson, C. Green, P. Clement, B. Zhi, A. Henke, E. Laudadio, S. E. Mason, R. Hamers, R. Klaper and C. Haynes, *Environ. Sci.: Nano*, 2020, DOI: 10.1039/C9EN01074B.



This is an Accepted Manuscript, which has been through the Royal Society of Chemistry peer review process and has been accepted for publication.

Accepted Manuscripts are published online shortly after acceptance, before technical editing, formatting and proof reading. Using this free service, authors can make their results available to the community, in citable form, before we publish the edited article. We will replace this Accepted Manuscript with the edited and formatted Advance Article as soon as it is available.

You can find more information about Accepted Manuscripts in the [Information for Authors](#).

Please note that technical editing may introduce minor changes to the text and/or graphics, which may alter content. The journal's standard [Terms & Conditions](#) and the [Ethical guidelines](#) still apply. In no event shall the Royal Society of Chemistry be held responsible for any errors or omissions in this Accepted Manuscript or any consequences arising from the use of any information it contains.

In manufacturing rechargeable lithium nickel manganese cobalt oxide-based batteries, industry is moving to formulations with increased nickel content, a component known to exhibit toxicity on environmental biota. Here we investigate the impact of these Ni-enriched materials to two environmentally relevant organisms, bacteria and a water flea. Due to the different toxicity mechanisms at play for these organisms, both respond differently to the industrial redesign strategy, with bacterial toxicity independent of material composition, but increasing toxicity to the water flea observed with increased nickel content. While this demonstrates that when redesigning nanomaterials, their impacts need to be tested on multiple organisms, it also shows the importance of understanding the relevant toxicity mechanisms to inform redesign strategies that mitigate overall environmental impact.

1  
2  
3 **Nickel enrichment of next-generation NMC nanomaterials alters material stability,**  
4 **causing unexpected dissolution behavior and observed toxicity to *S. oneidensis***  
5  
6

7 **MR-1 and *D. magna***  
8  
9

10  
11 Joseph T. Buchman<sup>§</sup>, Evan A. Bennett<sup>†</sup>, Chenyu Wang<sup>‡</sup>, Ali Abbaspour Tamijani<sup>||</sup>,  
12  
13 Joseph W. Bennett<sup>||</sup>, Blake G. Hudson<sup>||</sup>, Curtis M. Green<sup>‡</sup>, Peter L. Clement<sup>§</sup>, Bo Zhi<sup>§</sup>,  
14  
15 Austin H. Henke<sup>‡</sup>, Elizabeth D. Laudadio<sup>‡</sup>, Sara E. Mason<sup>||</sup>, Robert J. Hamers<sup>‡</sup>,  
16  
17 Rebecca D. Klaper<sup>†</sup>, Christy L. Haynes<sup>§</sup>  
18  
19

20  
21  
22  
23 <sup>§</sup>Department of Chemistry, University of Minnesota, Minneapolis, MN 55455, United  
24 States  
25  
26

27  
28 <sup>†</sup>School of Freshwater Sciences, University of Wisconsin-Milwaukee, Milwaukee, WI  
29 53204  
30  
31

32  
33 <sup>‡</sup>Department of Chemistry, University of Wisconsin, Madison, WI 53706, United States  
34  
35

36  
37 <sup>||</sup>Department of Chemistry, University of Iowa, Iowa City, Iowa 52242, United States  
38  
39  
40  
41  
42  
43  
44  
45  
46  
47  
48  
49  
50  
51  
52  
53  
54  
55  
56  
57  
58  
59  
60

## 1 2 3 1. Abstract 4 5

6  
7  
8  
9  
10  
11  
12  
13  
14  
15  
16  
17  
18  
19  
20  
21  
22  
23  
24  
25  
26  
27  
28  
29  
30  
31  
32  
33  
34  
35  
36  
37  
38  
39  
40  
41  
42  
43  
44  
45  
46  
47  
48  
49  
50  
51  
52  
53  
54  
55  
56  
57  
58  
59  
60  
Lithium intercalation compounds, such as the complex metal oxide, lithium nickel manganese cobalt oxide ( $\text{LiNi}_x\text{Mn}_y\text{Co}_{1-x-y}\text{O}_2$ , herein referred to as NMC), have demonstrated their utility as energy storage materials. In response to recent concerns about the global supply of cobalt, industrially synthesized NMCs are shifting toward using NMC compositions with enriched nickel content. However, nickel is one of the more toxic components of NMC materials, meriting investigation of the toxicity of these materials on environmentally relevant organisms. Herein, the toxicity of both nanoscale and microscale Ni-enriched NMCs to the bacterium, *Shewanella oneidensis* MR-1, and the zooplankton, *Daphnia magna*, was assessed. Unexpectedly, for the bacteria, all NMC materials exhibited similar toxicity when used at equal surface area-based doses, despite the different nickel content in each. Material dissolution to toxic species, namely nickel and cobalt ions, was therefore modelled using a combined density functional theory and thermodynamics approach, which showed an increase in material stability due to the Ni-enriched material containing nickel with an oxidation state  $>2$ . The increased stability of this material means that similar dissolution is expected between Ni-enriched NMC and equ stoichiometric NMC, which is what was found in experiments. For *S. oneidensis*, the toxicity of the released ions recapitulated toxicity of NMC nanoparticles. For *D. magna*, nickel enrichment increased the observed toxicity of NMC, but this toxicity was not due to ion release. Association of the NMC was observed with both *S. oneidensis* and *D. magna*. This work demonstrates that for organisms where the major mode of toxicity is based on ion release, including more nickel in NMC does not impact toxicity due to increased particle stability; however, for organisms where the core composition dictates the toxicity, including more nickel in the redesign strategy may lead to greater toxicity due to nanoparticle-specific impacts on the organism.

## 2. Introduction

Complex metal oxides are used in a variety of applications, such as catalysts or as cathode materials for lithium ion batteries.<sup>1,2</sup> Layered lithium-intercalation compounds such as lithium cobalt oxide,  $\text{LiCoO}_2$ , have been used as the primary cathode materials for lithium ion batteries for many years.<sup>3</sup> Recently, concerns about the diminishing global supply of cobalt has driven interest in exploring compositions that replace cobalt with nickel, manganese, and other more earth-abundant transition metals.<sup>4</sup> Therefore, materials of the general composition  $\text{LiNi}_x\text{Mn}_y\text{Co}_{1-x-y}\text{O}_2$ , here referred to as “NMC,” have been used because of the low cost of nickel and manganese compared to cobalt.

Increases in NMC commercialization lead to correspondingly larger manufacturing quantities and associated potential for environmental release.<sup>5</sup> Recent estimates predict that by 2025, worldwide manufacture of NMC materials will be between 136 kilotons/year and 330 kilotons/year.<sup>6</sup> While many present-generation cathodes use particles with primary sizes in the micron size range, nanoscale materials have been shown to improve certain performance characteristics such as charge rate.<sup>7-9</sup> As a result, nanoparticles (NPs) are increasingly being used in both cathode and anodes. Furthermore, even if micron-sized particles are used, weathering of electrodes during use leads to extensive fracturing and formation of much smaller particles, including those in the nanoparticle size regime.<sup>10-12</sup>

Within the family of NMC materials, the equ stoichiometric composition,  $\text{LiNi}_{1/3}\text{Mn}_{1/3}\text{Co}_{1/3}\text{O}_2$ , sometimes referred to as “333 NMC,”<sup>13,14</sup> is the most stable as it perfectly balances the preferred oxidation state of all three metal ions:  $\text{Ni}^{2+}$ ,  $\text{Mn}^{4+}$ , and  $\text{Co}^{3+}$ .<sup>13,15,16</sup> However, Ni-enriched formulations such as  $\text{LiNi}_{0.6}\text{Mn}_{0.2}\text{Co}_{0.2}\text{O}_2$  (622 NMC) and  $\text{LiNi}_{0.8}\text{Mn}_{0.1}\text{Co}_{0.1}\text{O}_2$  (811 NMC) are being rapidly commercialized. In order to balance the oxidation states, increases in nickel concentration lead to some of the nickel being present in the 3+ and 4+ oxidation states, which are highly reactive. As a result, such Ni-enriched NMC materials are expected to show unusual reactivity when compared to 333 NMC,<sup>17</sup> as high-valence cations tend to change the lattice

1  
2  
3 stability.<sup>18</sup> If such ions are released into aqueous media, they are also able to induce reactions  
4 such as the formation of reactive oxygen species (ROS). Because of the significant changes in  
5 stability and reactivity, many studies have been devoted to understanding how these changes  
6 impact the utilization of Ni-enriched NMC materials for energy storage. However, no prior  
7 studies have investigated how such nickel-enriched NMC compositions impact chemical  
8 transformations relevant to understanding the environmental impact of this class of materials.  
9 Given the large production of these nickel-enriched materials and higher probability of improper  
10 disposal due to the lack of recycling infrastructure for lithium ion batteries after their use,<sup>19</sup> there  
11 is a high likelihood that these battery materials will leach into the environment. This  
12 demonstrates the need for an investigation of the effects of nickel-enriched NMC on the  
13 environment upon release.  
14

15 Here, we report investigations of the impact of 333 and 622 NMC nanoparticles on two  
16 model organisms relevant to understanding the potential environmental impact that could result  
17 from release of these materials into the environment. Given the industrial relevance of these Ni-  
18 enriched materials, we also investigated the impact of commercially available Ni-enriched NMC  
19 materials, which are detailed in the ESI. Both *Shewanella oneidensis* MR-1 and *Daphnia magna*  
20 are aquatic organisms that represent different trophic levels. In this work, they are used as  
21 model organisms for assessing environmental impact, due to the fact that their ubiquitous  
22 presence in a range of aquatic environments makes them likely to be exposed to NMC in the  
23 event of aquatic introduction. *S. oneidensis* is capable of respiring many different metals in its  
24 environment,<sup>20</sup> and *D. magna* are an important component of the freshwater food web and are  
25 sensitive to many environmental pollutants.<sup>21</sup> Daphnids are a parthenogenetic organism and  
26 therefore maintain nearly identical genetic composition throughout a population, which makes  
27 them ideal for experimentation. Density functional theory (DFT) modeling of Ni-rich formulations  
28 is carried out, and ion release is modeled using a DFT + solvent ion model based on Hess's  
29  
30  
31  
32  
33  
34  
35  
36  
37  
38  
39  
40  
41  
42  
43  
44  
45  
46  
47  
48  
49  
50  
51  
52  
53  
54  
55  
56  
57  
58  
59  
60

law.<sup>22,23</sup> Additionally, calculations that take into account complexation of released ions are carried out to offer further interpretation of the experimental dissolution data.

Contrary to expectations, our results show that at matching surface area-based doses, the different NMC nanoparticles studied here yielded similar toxicity to our bacterial model, *S. oneidensis*. Dissolution analysis reveals that the 333 and 622 NMC compositions studied release nickel and cobalt ions, which are known to be toxic to *S. oneidensis*, at approximately the same rate. In contrast, with *D. magna*, nanoparticles with the nickel-enriched 622 NMC composition exhibited a higher toxicity than those with the equ stoichiometric 333 NMC composition. The complementary theoretical studies provide insights into how composition-dependent changes in oxidation states, as well as the thermodynamics of complexation reactions in water, influence the dissolution profiles. This comparative work demonstrates the importance of using multiple organisms to assess environmental toxicity of a nanoparticle, and shows how the same strategy to redesign a nanomaterial can have different organismal impacts based on the nanoparticle toxicity mechanism.

### 3. Experimental

#### 3.1 Materials

Nickel (II) chloride hexahydrate ( $\text{NiCl}_2 \cdot 6\text{H}_2\text{O}$ ), magnesium chloride ( $\text{MgCl}_2$ ), ammonium chloride ( $\text{NH}_4\text{Cl}$ ), calcium chloride ( $\text{CaCl}_2$ ), hydrogen peroxide ( $\text{H}_2\text{O}_2$ ), 4'-aminophenyl fluorescein (APF), and 2',7'-dichlorofluorescin diacetate ( $\text{H}_2\text{DCF-DA}$ ) were purchased from Thermo Fisher Scientific (Waltham, MA). Sodium chloride ( $\text{NaCl}$ ), sodium sulfate ( $\text{Na}_2\text{SO}_4$ ), dibasic sodium phosphate ( $\text{Na}_2\text{HPO}_4$ ), 4-(2-hydroxyethyl)-1-piperazineethanesulfonic acid (HEPES), dimethylsulfoxide (DMSO), manganese (II) nitrate tetrahydrate ( $\text{Mn}(\text{NO}_3)_2 \cdot 4\text{H}_2\text{O}$ ), cobalt (II) nitrate hexahydrate ( $\text{Co}(\text{NO}_3)_2 \cdot 6\text{H}_2\text{O}$ ), and lithium nitrate ( $\text{LiNO}_3$ ) were obtained from Sigma-Aldrich (St. Louis, MO). Manganese (II) sulfate monohydrate ( $\text{MnSO}_4 \cdot \text{H}_2\text{O}$ ), cobalt (II) chloride hexahydrate ( $\text{CoCl}_2 \cdot 6\text{H}_2\text{O}$ ), and potassium chloride (KCl) were acquired from Mallinckrodt (St. Louis, MO). Propylene oxide and 10% glutaraldehyde in water were purchased from Electron Microscopy

Sciences (Hatfield, PA). Poly/Bed® 812 resin kit was obtained from Polysciences, Inc. (Warrington, PA). A horseradish peroxidase (HRP) solution containing Triton-X and cholate, came from an amplex red kit that was acquired from Cayman Chemical (Ann Arbor, MI). Absolute ethanol was purchased from Pharmco-Aaper (Brookfield, CT). Sodium lactate and nickel (II) nitrate hexahydrate ( $\text{Ni}(\text{NO}_3)_2 \cdot 6\text{H}_2\text{O}$ ) were purchased from Alfa Aesar (Haverhill, MA). Lithium hydroxide monohydrate ( $\text{LiOH} \cdot \text{H}_2\text{O}$ ) was obtained from VWR (Radnor, PA). Luria-Bertani broth and agar were purchased from BD Difco (Franklin Lakes, NJ). Ultrapure water (18.2  $\text{M}\Omega \cdot \text{cm}$  resistivity) was purified from a Milli-Q Millipore water purification system (Billerica, MA). *S. oneidensis* MR-1 BAA1096 was purchased from the American Type Culture Collection (Manassas, VA). *D. magna* were originally acquired from Aquatic Research Organisms (Hampton, NH) and were then maintained in the lab of Dr. Rebecca Klaper at the University of Wisconsin-Milwaukee School of Freshwater Sciences following guidelines described by the US EPA.

### 3.2 Synthesis of NMC nanoparticles

NMC nanoparticles were synthesized using a two-step procedure. First, a nickel manganese cobalt hydroxide precursor was synthesized via a co-precipitation technique in which an aqueous mixture of 0.2 M  $\text{Ni}(\text{NO}_3)_2 \cdot 6\text{H}_2\text{O}$ , 0.2 M  $\text{Mn}(\text{NO}_3)_2 \cdot 4\text{H}_2\text{O}$ , and 0.2 M  $\text{Co}(\text{NO}_3)_2 \cdot 6\text{H}_2\text{O}$  was added dropwise to 0.2 M LiOH under magnetic stirring. To make NMC nanosheets, the following concentrations were instead used: 0.3 M  $\text{Ni}(\text{NO}_3)_2 \cdot 6\text{H}_2\text{O}$ , 0.1 M  $\text{Mn}(\text{NO}_3)_2 \cdot 4\text{H}_2\text{O}$ , and 0.1 M  $\text{Co}(\text{NO}_3)_2 \cdot 6\text{H}_2\text{O}$ . A dark brown precipitate of metal hydroxides was collected via repeated cycles of centrifugation (Thermo Scientific Sorvall Legend X1R centrifuge with Thermo TX-400 rotor, 4696 $\times g$ ) and resuspension in water (1 $\times$ ) and methanol (4 $\times$ ) followed by drying under vacuum at 30 °C. This metal hydroxide precursor (~500 mg) was then added to a 10 g molten flux containing 6:4 molar ratio of  $\text{LiNO}_3$ :LiOH at 230 °C in a high-alumina crucible. The reaction was quenched after 3 hours using ultrapure water, producing NMC with a nanosheet morphology. These nanosheets were isolated using repetitive cycles of

1  
2  
3 centrifugation at 4696×g and resuspension in water (2×) and methanol (3×) and dried under  
4 vacuum at 30 °C. The collected pellets were ground into a fine powder using an agate mortar  
5 and pestle. These purified nanoparticles were characterized using powder X-ray diffraction  
6 (XRD), inductively coupled plasma optical emission spectrometry (ICP-OES) to determine NMC  
7 stoichiometry, scanning electron microscopy, and nitrogen physisorption prior to being used for  
8 ion release and toxicity studies.

### 9 **3.3 Characterization of NMC Stoichiometry**

10 To analyze the chemical composition of both synthesized 333 and 622 NMC nanosheets, a  
11 PerkinElmer 4300 Dual View inductively coupled plasma optical emission spectrometer was  
12 used. First, solid materials were completely dissolved in freshly-made aqua regia (3:1 v/v  
13 mixture consisting of 37% v/v HCl and 70% v/v HNO<sub>3</sub>; *caution: aqua regia is highly corrosive!*)  
14 through soaking overnight. Then the dissolved contents were diluted with ultrapure water and  
15 analyzed. The standards were prepared using a certified reference solution and the blank was  
16 2% aqua regia aqueous solution. The ion concentrations were measured using three analytical  
17 replicates.

### 18 **3.4 TEM and EDS of NMC**

19 To acquire TEM images of the samples, the stock NMC materials were suspended in ultrapure  
20 water at 500 ppm and sonicated for 10 min to ensure dispersal. Afterward, 2 µL drops were  
21 placed on a 200 mesh TEM grid made of copper with Formvar and carbon supports (Ted Pella,  
22 Inc., Redding, CA). The grids were allowed to dry overnight prior to using an FEI Tecnai T12  
23 TEM to acquire images at an operating voltage of 120 kV.

24 To determine the ratio of transition metals in each NMC material, energy-dispersive X-ray  
25 spectroscopy (EDS) was used. EDS spectra for the materials were acquired with an Oxford  
26 INCAx-sight EDS that was paired with the T12 TEM. TEM was used to focus on the NMC  
27 material, and then EDS was acquired for 0-10 keV with an ultrathin window Si(Li) detector. The  
28 ratios of the transition metals in each material were determined using the atomic percentages

1  
2  
3 reported by EDS.  
4  
5

### 6 3.5 Surface Area Measurements

7 The Brunauer-Emmett-Teller (BET) specific surface areas of 333 and 622 NMC nanosheets  
8 were determined using  $N_2$  adsorption/desorption isotherms obtained from a Micromeritics  
9 Gemini VII 2390 surface area analyzer. Each sample holder (Micromeritics) was loaded with  
10 ~70 mg of powder and outgassed at 120 °C under vacuum for 1 h using a Micromeritics  
11 VacPrep 061 sample degas system. The sample was subsequently introduced into the surface  
12 area analyzer and measured over the relative pressure range ( $P/P_0$ ) of 0.05–0.3, where  $P_0$  is  
13 the saturated pressure of  $N_2$ .  
14  
15

### 16 3.6 Zeta Potential of NMC in Exposure Media

17 To determine the  $\zeta$ -potential of NMC in the exposure media, each NMC sample was suspended  
18 in either bacterial medium or daphnid medium at a concentration of 25 ppm.  $\zeta$ -potential  
19 measurements were acquired using a Brookhaven ZetaPALS instrument.  
20  
21

### 22 3.7 Bacterial Culture Conditions

23 *S. oneidensis* MR-1 BAA1096 was stored at -80 °C until needed. Then, the bacterial suspension  
24 was streaked onto a sterile LB agar plate and incubated overnight at 30 °C. Two colonies were  
25 inoculated in LB broth and incubated for ~16 hr (300 rpm, 30 °C). The bacteria in late log phase  
26 were centrifuged at 750×g for 10 min and resuspended in 0.85% NaCl. They were again  
27 centrifuged (10 min, 750×g) and resuspended in bacterial medium (composed of 11.6 mM NaCl,  
28 4.0 mM KCl, 1.4 mM MgCl<sub>2</sub>, 2.8 mM Na<sub>2</sub>SO<sub>4</sub>, 2.8 mM NH<sub>4</sub>Cl, 88.1  $\mu$ M Na<sub>2</sub>HPO<sub>4</sub>, 50.5  $\mu$ M CaCl<sub>2</sub>,  
29 10 mM HEPES, and 100 mM sodium lactate). The OD<sub>600</sub> was determined and adjusted as  
30 needed.  
31  
32

### 33 3.8 Bacterial Growth-based Viability Assays

34 To determine the toxicity of the NMC samples to *S. oneidensis*, a previously published growth-  
35 based viability assay protocol was adapted.<sup>24</sup> Stock suspensions of NMC were prepared to be  
36 at 10× the exposure concentration and then sonicated for 10 min to ensure dispersity. Briefly,  
37 the OD<sub>600</sub> of *S. oneidensis* in bacterial medium was adjusted to 0.1 and then exposed to 333  
38  
39  
40  
41  
42  
43  
44  
45  
46  
47  
48  
49  
50  
51  
52  
53  
54  
55  
56  
57  
58  
59  
60

and 622 NMC at surface area-based concentrations ranging from 0-2.8 m<sup>2</sup>/L in a 96-well plate for 3 hours with agitation (for ion controls, the bacteria were exposed to mixtures of Li<sup>+</sup>, Ni<sup>2+</sup>, Mn<sup>2+</sup>, and Co<sup>2+</sup> ions at their measured released concentrations from ICP-MS studies). In parallel, a calibration curve was set up using the stock bacterial suspension and diluting 1:1 with bacterial medium to get a range from 6.25-100% viable. After exposure, 5 µL of each suspension was diluted into 195 µL of fresh LB broth and OD<sub>600</sub> was measured using a Biotek Synergy™ 2 multi-mode microplate reader, taking measurements every 20 min after 30 s shaking overnight. The resulting growth curves were analyzed using the R package provided by Qiu et al (2017) to determine the bacterial viability post-exposure.<sup>24</sup>

### 3.9 *D. magna* Culture Maintenance

*D. magna* were kept in moderately hard reconstituted water (daphnid medium), which was produced at 2× concentrations and diluted to 96 mg/L NaHCO<sub>3</sub>, 60 mg/L CaSO<sub>4</sub>, 60 mg/L MgSO<sub>4</sub>, 4 mg/L of KCl, and 0.02 mL/L of Na<sub>2</sub>SeO<sub>3</sub>•5H<sub>2</sub>O (added using a 330 mg/L Na<sub>2</sub>SeO<sub>3</sub>•5H<sub>2</sub>O solution). The medium was aerated with an air stone for 48 hours before use. The cultures were kept at a population density of 20 adult daphnids/L in an incubator at 20 °C with a 16:8 light:dark cycle. The cultures were fed three times a week using 25 mL of algae (*Raphidocelis subcapitata*, 500,000 algal cells/mL) as well as 10 mL of alfalfa (*Medicago sativa*) supernatant (prepared by suspending 8 grams in 1 L of Milli-Q water and agitating the suspension for 20 min at 130 rpm on a Thermo Scientific MaxQ 4450 orbital shaker).

### 3.10 *Daphnia magna* Acute Toxicity Assays

*Daphnia* were exposed to 333 and 622 NMC by exposing them to 2× concentrated stock suspensions (for ion controls, stocks containing a mixture Li<sup>+</sup>, Ni<sup>2+</sup>, Mn<sup>2+</sup>, and Co<sup>2+</sup> ions at the concentrations determined to be released by ICP-MS were instead used). The stock had been sonicated for 10 minutes immediately prior to use. *D. magna* neonates (<24 hours old) from adults aged 14-28 days were placed in 10 mL solutions (comprised of 5 mL of 2× daphnid medium, and a combination of NMC stock for desired nanoparticle concentration, and Milli-Q

water). The NMC nanoparticles were tested at concentrations ranging from 0-2.8 m<sup>2</sup>/L. Exposures included 4 replicates per treatment with 5 neonates per replicate, and acute toxicity tests were conducted as per OECD guideline 202 with the assays being run for 48 hours with no food supplementation during this time. Survival was recorded after 24 and 48 hours.

Images of the *D. magna* were taken on an Evos XL Core Cell Imaging System to visualize the association of NMC with the daphnids. Live *D. magna* were photographed immediately following the 48-hour exposure to the various NMC materials. Images were analyzed using ImageJ software.

### 3.11 Computational Modeling of Cation Release from Ni-enriched NMC

Density functional theory (DFT) calculations<sup>25,26</sup> of Ni-enriched NMC surface structures use the open source software package, Quantum Espresso.<sup>27</sup> All atoms are represented using ultrasoft GBRV-type pseudopotentials,<sup>28,29</sup> and all calculations employ a plane-wave cutoff of 40 Ry for the wavefunction and 320 Ry for the charge density. All atoms are allowed to relax during structural optimizations, and the convergence criteria for all self-consistent relaxations was a maximum residual force of 5 meV/Å per atom. Calculations are performed at the DFT-GGA level using the PBE exchange correlation functional.<sup>30</sup>

Ni-enriched NMC surface slabs used here include four total O-TM-O layers, like the NMC surfaces modeled in previous work (more information can be found in the ESI).<sup>22,31</sup> For the  $2\sqrt{3} a \times \sqrt{3}a$  cells, we investigate two Ni-enriched NMC compositions:  $\text{Li}_x\text{Ni}_{2/6}\text{Mn}_{2/6}\text{Co}_{2/6}\text{O}_2$  (33% Ni, 33% Mn, 33% Co) denoted as 333 NMC, and  $\text{Li}_x\text{Ni}_{4/6}\text{Mn}_{1/6}\text{Co}_{1/6}\text{O}_2$  (66% Ni, 17% Mn, 17% Co) which will be denoted as 622 NMC. Note that this is not exactly the same stoichiometry as the 622 NMC used in the exposure experiments, but since each of these has six total transition metal sites, it simplifies the calculations to list the stoichiometry based on six atoms. Because there are six total transition metal sites, release of 1 transition metal from the surface results in a vacancy density of 1/6 or 16.67%. For the  $3\sqrt{3}a \times \sqrt{3}a$  cells, we investigated two Ni-enriched NMC compositions:  $\text{Ni}_{3/9}\text{Mn}_{3/9}\text{Co}_{3/9}$  (33% Ni, 33% Mn, 33% Co) denoted as 333 NMC, and

<sup>1</sup>  
<sup>2</sup>  
<sup>3</sup>  $\text{Ni}_{7/9}\text{Mn}_{1/9}\text{Co}_{1/9}$  (78% Ni, 11% Mn, 11% Co) denoted as 811 NMC. Each of these has 9 total  
<sup>4</sup> transition metal sites, so release of 1 transition metal from the surface results in a vacancy  
<sup>5</sup> density of 1/9 or 11.11%.  
<sup>6</sup>  
<sup>7</sup>

<sup>8</sup>  
<sup>9</sup> For the 622 with 6 transition metal sites (622-A) and 333 compositions, we investigate one  
<sup>10</sup> distinct arrangement, and for the 811 NMC compositions, we investigate two distinct  
<sup>11</sup> arrangements which are labeled A and B. These surfaces are shown in Figure 1 and form a  
<sup>12</sup> representative set in which the oxidation state and coordination environment (via atomistic  
<sup>13</sup> interactions such as neighboring atoms and surface terminations) can be compared. Each  
<sup>14</sup> transition metal removed will have a subscript with the number of nickel nearest neighbors and  
<sup>15</sup> a superscript with the number of manganese and/or cobalt nearest neighbors.  
<sup>16</sup>  
<sup>17</sup>

<sup>18</sup>  
<sup>19</sup> For example, removing the cobalt from 811-A with 4 nickel and 2 manganese neighbors  
<sup>20</sup> (depicted in Figure 1) would be referred to as removing 811-A- $\text{Co}_{4\text{Ni}}^{2\text{Mn}}$ , and this structure is  
<sup>21</sup> distinct from one when removing the cobalt from 811-B with 6 nickel neighbors (depicted in  
<sup>22</sup> Figure 1), which would be referred to as 811-B- $\text{Co}_{6\text{Ni}}^{0\text{Mn}}$ . It should be noted that not every  
<sup>23</sup> transition metal is removed from each Ni-enriched surface, but only a small set to map out the  
<sup>24</sup> breadth of metal release from a complex metal oxide. The initial steps of dissolution are  
<sup>25</sup> modeled as surface metal release by releasing a transition metal (TM), O, and H from the  
<sup>26</sup> surface. In the DFT calculations, we assume that lattice transition metals will undergo oxidation,  
<sup>27</sup> in a possibly delocalized fashion, upon removal of a TM-OH unit. Under this assumption, the  
<sup>28</sup> defect slab model is charge neutral, exhibiting (possibly partially) oxidized transition metals  
<sup>29</sup> relative to the pristine slab. Which transition metals oxidize, and to what extent, is based on the  
<sup>30</sup> DFT charge density. The changes in transition metal oxidation states in the slab mode as a  
<sup>31</sup> function of vacancy formation is in line with how the transition metals are thought to oxidize and  
<sup>32</sup> reduce during the operation (charge/discharge) of a Li-ion battery.  
<sup>33</sup>  
<sup>34</sup>  
<sup>35</sup>  
<sup>36</sup>  
<sup>37</sup>  
<sup>38</sup>  
<sup>39</sup>  
<sup>40</sup>  
<sup>41</sup>  
<sup>42</sup>  
<sup>43</sup>  
<sup>44</sup>  
<sup>45</sup>  
<sup>46</sup>  
<sup>47</sup>  
<sup>48</sup>  
<sup>49</sup>  
<sup>50</sup>  
<sup>51</sup>  
<sup>52</sup>  
<sup>53</sup>  
<sup>54</sup>  
<sup>55</sup>  
<sup>56</sup>  
<sup>57</sup>  
<sup>58</sup>  
<sup>59</sup>  
<sup>60</sup>

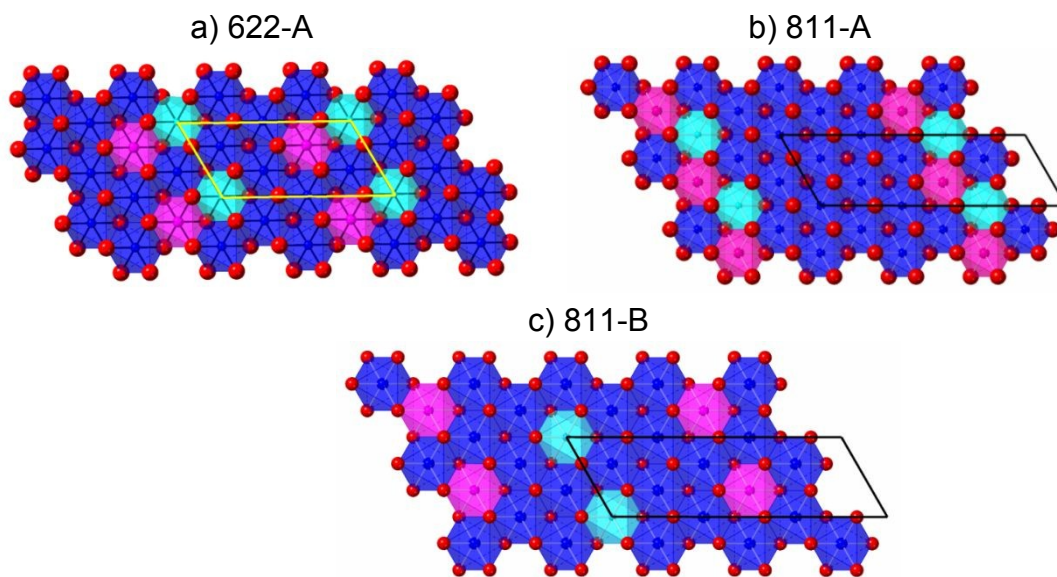


**Figure 1. Computational models of Ni-enriched NMC surfaces with different stoichiometries.** Top-down views of the a) 622 and b, c) 811 Ni-enriched NMC surfaces. The supercell slab repeat units are highlighted with yellow and black lines for the 622 and 811 compositions, respectively, to show the different size repeat units. For the 811 Ni-enriched NMC surfaces the distance between manganese (magenta) and cobalt (cyan) octahedra is changed from b) nearest neighbor to c) manganese and cobalt separated by two nickel atoms.

To compute the thermodynamics of metal release, the change in free energy of dissolution,  $\Delta G_{\text{diss}}$ , was computed using methodology that combines first-principles DFT and thermodynamics. This DFT + solvent ion method<sup>23,32</sup> is based on Hess's Law, where  $\Delta G_{\text{diss}}$  is partitioned between the DFT-computed total energies of the reactants and products (used as  $\Delta G_1$ ) and experimental data (used as  $\Delta G_2$ ).

One of the main objectives of this work is to investigate the release of metals from Ni-enriched NMC materials for a range of environmentally relevant conditions. Choosing a wide pH range allows for release comparisons of divalent transition metal cation species  $\text{Ni}^{2+}$ ,  $\text{Mn}^{2+}$ , and  $\text{Co}^{2+}$  in many diverse aquatic environments. Example calculations of  $\Delta G_{\text{diss}}$  from NMC materials are presented in the supplemental materials of previous work.<sup>22,31</sup>

The computational modeling here can be extended to take into account complexing reactions likely to occur in the different growth media. The calculations presented above consider ion release in pure water, and the model divides the process into two steps that

contribute to the overall  $\Delta G_{\text{diss}}$ : the first term is the energy penalty to remove cations from the lattice structure ( $\Delta G_1$ ). The second term is the energy given off upon solvation of now-released cation ( $\Delta G_2$ ). However, experimental data reveals that the presence of lactate (LA) facilitates the release process. To theorize the effect of the presence of lactate on the dissolution process, we introduce a third term to the model that accounts for the chelation of lactate to the solvated cation ( $\Delta G_3$ ). This last term is formed by considering the ligand exchange occurring between the hexa-aqua cation complex and lactate anion ( $TM = \text{Co, Ni, Mn}$ ):



or



Values of  $\Delta G_3$  are calculated based on (ZPE corrected) DFT total energy values of reaction products minus reactants, where all values are weighted appropriately by stoichiometry. As  $\Delta G_3$  calculations are reported as energy differences, there is no need for the same computational methods used in  $\Delta G_1$  calculations to be used. In fact,  $\Delta G_3$  calculations involve modeling isolated molecular species in water, which are not systems that are well-suited for the planewave periodic DFT methods used for calculating  $\Delta G_1$ . All the  $\Delta G_3$  calculations are performed using DMol<sup>3</sup> software.<sup>33,34</sup> PBE<sup>30</sup> and B3LYP<sup>35</sup> functional types were used along with DNP basis functions, truncated at 4.5 Å, employed to describe the atomic species (A comparison of  $\Delta G_3$  values determined by PBE and B3LYP can be found in ESI). All calculations are carried out in an implicitly solvated environment (COSMO) with water as the solvent. Spin-polarized calculations are carried out to account for the unpaired spin of the 2+ oxidation states of nickel, manganese, and cobalt.

### 3.12 Ion Dissolution from NMC

To empirically measure dissolution from the NMC materials in bacterial medium, the NPs were suspended in bacterial medium so that their surface area-based concentrations ranged from

0.18-2.8 m<sup>2</sup>/L and were agitated over the course of 3 hours. For measurements in daphnid medium, the NPs were suspended in glass vials (concentrations ranging from 0.18-2.8 m<sup>2</sup>/L), and kept at 20 °C for 48 hours. After the exposure times for each media, the majority of the materials were removed by centrifugation at 4696×g for 30 min using a Beckman Coulter Allegra® X-15R centrifuge. The supernatant was then transferred to an ultracentrifuge tube and centrifuged at 286,000×g for one hour in an SW 55 Ti rotor on the Beckman Coulter Optima™ L-100K Ultracentrifuge. To verify that the NMC material had sedimented, and was therefore not present in the supernatant, dynamic light scattering (Brookhaven Instruments ZetaPALS zeta potential analyzer) was used. The bacterial medium supernatants were then diluted 10-fold and analyzed with a Thermo Scientific Xseries-2 ICP-MS. The supernatants from the daphnid medium were analyzed with a Thermo Scientific Element XR ICP-MS without dilution.

To investigate how the presence of lactate in the bacterial medium impacts dissolution, NMC materials were suspended in bacterial medium with and without lactate to a surface area-based concentration between 3.0-4.1 m<sup>2</sup>/L and agitated for 24 hours. After the exposure times for each media, the materials were removed by centrifugation at 64,000×g for 20 minutes in a JA 25.50 rotor on the Beckman Avanti J-25 centrifuge. The supernatants were diluted 2-fold and analyzed with a PerkinElmer Optima 4300 Dual View ICP-OES.

### 3.13 Abiotic ROS Determination for 333 and 622 NMC Nanosheets

To measure abiotic production of reactive oxygen species from 333 and 622 NMC and their released ions in both bacterial medium and daphnid medium, a previously published method was utilized.<sup>36,37</sup> In this procedure, two fluorescent probes were employed: 3'-aminophenyl fluorescein (APF), which measures hydroxyl radical generation, and 2',7'-dichlorofluorescin diacetate (H<sub>2</sub>DCF-DA), which measures overall ROS production. The dyes have excitation and emission wavelengths of 495 nm/525 nm and 500 nm/530 nm, respectively. To first deacetylate the H<sub>2</sub>DCF-DA prior to exposing to NMC, it was diluted by mixing 20 mM of H<sub>2</sub>DCF-DA in anhydrous DMSO in a 1:1 ratio with 0.1 M NaOH in appropriate medium and letting it sit in the

dark for 30 minutes. To prepare working solutions of the dyes, APF (at 5 mM in DMF) and the base-treated H<sub>2</sub>DCF-DA were diluted 50-fold and 100-fold, respectively, to achieve 100  $\mu$ M solutions in medium. Horseradish peroxidase (HRP) was prepared by doing a 100-fold dilution of the 1300 U/mL HRP stock into medium. An 88  $\mu$ M stock of H<sub>2</sub>O<sub>2</sub> in medium was also prepared beforehand. To their respective wells, combinations of the following were added, in this order, to give 100  $\mu$ L per exposure: appropriate medium, 10  $\mu$ L of dye working solution, 10  $\mu$ L of 2.849 m<sup>2</sup>/L 333 or 622 NMC suspension or their respective ion concentrations, 10  $\mu$ L of HRP solution, and 10  $\mu$ L of H<sub>2</sub>O<sub>2</sub> solution. The combinations were as follows: i. negative control (dye, medium); ii. positive control (dye, HRP, H<sub>2</sub>O<sub>2</sub>, medium); iii. partial positive control #1 (dye, HRP, medium); iv. partial positive control #2 (dye, H<sub>2</sub>O<sub>2</sub>, medium); v. NMC exposure (dye, NMC, medium); and vi. NMC positive control interference check (dye, NMC, HRP, H<sub>2</sub>O<sub>2</sub>, medium). Given that production of ROS is related to the dissolution of NMC, and that most of the NMC dissolution occurs in the first few hours after being added to aqueous media,<sup>38</sup> the exposures were done for 3 hours prior to reading optical density at 600 nm and fluorescence at the appropriate excitation/emission wavelengths.

### 3.14 Association of NMC to *S. oneidensis* MR-1 using TEM and CytoViva Analysis

To take TEM images of the bacteria that had been exposed to NMC, the NMC-exposed bacterial samples were embedded in an epoxy resin using an adapted method.<sup>39,40</sup> Briefly, the bacteria were adjusted to an optical density of 0.8 in bacterial medium and then exposed to 333 and 622 NMC at 12.5 ppm for 60 minutes on a nutating mixer. The cells were then washed in 0.1 M cacodylate buffer three times prior to being fixed for 50 minutes in 2.5% glutaraldehyde in 0.1 M cacodylate buffer; the pellet was flipped after 25 min to ensure complete fixation. Afterward, the pellet was again washed three times (without resuspension) in 0.1 M cacodylate buffer.

The bacteria were then dehydrated, washing for 5 min each with ethanol at increasing % v/v (30%, 50%, 70%, 80%, 95%, and 100% ethanol in water). Propylene oxide was used to rinse

1  
2  
3 three times, and then the pellet was incubated uncovered at room temperature for 2 hours with  
4 a 2:1 propylene oxide:resin mix (samples were covered for subsequent incubations). Incubation  
5 with a 1:1 propylene oxide:resin mixture was then performed overnight, which was replaced with  
6 fresh 1:1 propylene oxide:resin for 4 hours. The pellet was then incubated with pure resin  
7 overnight. This was then replaced with fresh resin and then the samples were incubated at 40  
8 °C for 24 hours following by incubation at 60 °C for 48 hours. A LEICA EM UC6 ultramicrotome  
9 was used to cut the samples into ~70-nm-thick sections, which were then stained with uranyl  
10 acetate and lead citrate for improved contrast. The sections were placed on 200 mesh copper  
11 grids that have Formvar and carbon supports (TedPella Inc, Redding, CA); images were  
12 acquired with a Tecnai T12 transmission electron microscope at an operating voltage of 120 kV.  
13  
14

15 The association between *Shewanella oneidensis* MR-1 and various NMC battery materials  
16 was also analyzed using CytoViva enhanced darkfield microscopy and hyperspectral  
17 microscopy (CytoViva Inc., Auburn, AL). The entire system is composed of an upright optical  
18 microscope (Olympus BX43), a visible-near infrared CytoViva hyperspectral imaging system,  
19 and a halogen light source. Reference samples are a bacterial culture suspension in bacterial  
20 medium (OD = 0.60) and NMC suspensions in water (25 mg/L 333 NMC and 25 mg/L 622  
21 NMC), which were used for spectral library construction; samples that were subject to  
22 hyperspectral mapping were bacterial suspensions that had been exposed for 1 h to different  
23 NMC materials. To mount the specimen, live bacterial exposure suspensions were drop-cast  
24 (~3 µL) onto a glass slide and then sealed with a coverslip. Slides were examined under 100x  
25 magnification darkfield and subsequent line-by-line hyperspectral scanning (ENVI 4.8 software)  
26 was performed using 60-80% light source intensity and 0.25 s exposure time per line (696 lines  
27 in total for a typical full scan). Each pixel of the hyperspectral image (i.e., 3D datacube) contains  
28 its spatial information (x and y) and corresponding reflectance spectral data (z). Analysis of  
29 hyperspectral data (mapping) was performed using Spectral Angle Mapper Classification  
30 (SAM), which automatically compared the hyperspectral data of NMC-exposed bacteria to the  
31  
32  
33  
34  
35  
36  
37  
38  
39  
40  
41  
42  
43  
44  
45  
46  
47  
48  
49  
50  
51  
52  
53  
54  
55  
56  
57  
58  
59  
60

reference libraries and identified different components. Pixels in the images that matched the reference libraries were pseudo-colored in red (*S. oneidensis*) and green (NMC materials).

## 4. Results and Discussion

### 4.1 Synthesis and Characterization of NMC materials

After synthesis of the NMC nanoparticles, their stoichiometry was measured by dissolving the nanoparticles and measuring the amount of each element using ICP-OES. This showed the composition of the 333 NMC nanoparticles to be  $\text{Li}_{0.63}\text{Ni}_{0.34}\text{Mn}_{0.33}\text{Co}_{0.33}\text{O}_2$  and the 622 NMC nanoparticles to be  $\text{Li}_{0.31}\text{Ni}_{0.60}\text{Mn}_{0.20}\text{Co}_{0.20}\text{O}_2$ , which meets the expected transition metal stoichiometries for these materials. EDS corroborates the stoichiometries observed for the nanoparticles. From EDS, we see the following stoichiometries for 333 NMC and 622 NMC:  $\text{Li}_x\text{Ni}_{0.29}\text{Mn}_{0.37}\text{Co}_{0.34}\text{O}_2$  and  $\text{Li}_x\text{Ni}_{0.59}\text{Mn}_{0.21}\text{Co}_{0.20}\text{O}_2$ ; note that lithium was not quantified due to limitations of EDS.<sup>41</sup> Both TEM and SEM images of the nanosheets depict the sheet-like morphology of these materials and that there is a range of sizes present in each sample (see ESI). The surface areas of the nanoparticles were determined to be very similar, with 333 NMC and 622 NMC having surface areas of 114.0 m<sup>2</sup>/g and 107.3 m<sup>2</sup>/g, respectively. These surface areas were used to inform the surface-area based dosing of NMC to *S. oneidensis* MR-1 and *D. magna*.  $\zeta$ -potential measurements revealed that the nanoscale materials exhibited a less negative surface charge in both bacterial medium and in daphnid medium (Table S1) than the commercially available NMC materials.

### 4.2 Toxicity of NMC materials to *S. oneidensis* MR-1

To analyze the toxicity of NMC to *S. oneidensis*, the bacteria were exposed to the material for 3 h, and then viability was measured using a growth-based viability assay. Throughout the exposure, the samples were shaken to keep the nanoparticles and bacteria in suspension, but no effort was made to control the aggregation state of the NMC, as aggregation is expected in environmental settings. Unexpectedly, both nanoparticles demonstrated similar toxicity to *S. oneidensis*, regardless of nickel content (Figure 2); surprisingly, similar toxicity was also

observed with *S. oneidensis* when exposed to the commercial, microscale NMC materials, which had even further enriched nickel content than the nanoscale materials (Figure S6). It was expected that, since nickel and cobalt are the main contributors of NMC toxicity to these bacteria, there would be more nickel available from the Ni-enriched NMC materials and they would therefore exhibit an increased toxicity. These unexpected results prompted further investigation of the toxicity mechanisms of NMC materials of different compositions, to determine if any novel mechanisms were contributing to the toxicity of the nickel-enriched NMC compositions.

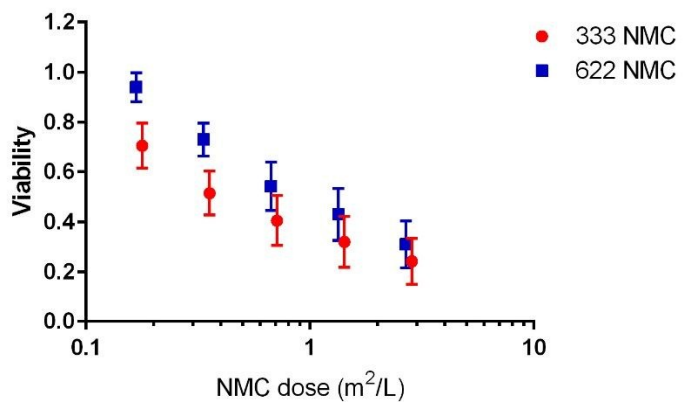


**Figure 2. Surface area-based dosing of NMC materials to *S. oneidensis* demonstrates that toxicity of equ stoichiometric and Ni-enriched NMC materials is similar. The error bars represent the standard error of seven replicates. To test for statistical significance, a one-way ANOVA with Tukey's multiple comparisons test was used on calculated LD50 values for each material.**

#### 4.3 Cation Release from Ni-enriched NMC

Using a theoretical approach to investigate material dissolution, here we discuss computationally predicted metal release trends from the surface, using the  $\Delta G_{\text{diss}}$  values in Table 1. In general, the metal release rates observed experimentally correlate to the trends in  $\Delta G_{\text{diss}}$ , where the order is Ni>Co>Mn. Also  $\Delta G_{\text{diss}}$  increases (toward positive values) as the percent of released metal increases from 11.11 to 16.67%. This indicates that the surface release may not be energetically favorable above a certain TM-OH vacancy threshold. The data

in Table 1 show that for nickel, cobalt, and manganese, release of 11.11% of the surface metal at pH 6 is thermodynamically favored, but at 16.67%, only nickel is predicted to be released.

**Table 1.  $\Delta G_{\text{diss}}$  at pH 6 for nickel, cobalt, and manganese at different surface vacancy concentrations.**

Cation	% Vacancy	$\Delta G$ (eV)
811-A- $\text{Ni}_{6\text{Ni}}^{0\text{Mn} - 0\text{Co}}$	11.11	-2.97
811-B- $\text{Ni}_{4\text{Ni}}^{2\text{Mn} - 0\text{Co}}$	11.11	-2.82
811-A- $\text{Ni}_{3\text{Ni}}^{2\text{Mn} - 1\text{Co}}$	11.11	-2.64
811-B- $\text{Ni}_{5\text{Ni}}^{0\text{Mn} - 1\text{Co}}$	11.11	-2.47
333-A- $\text{Ni}_{0\text{Ni}}^{3\text{Mn} - 3\text{Co}}$	11.11	-2.11
622-A- $\text{Ni}_{4\text{Ni}}^{1\text{Mn} - 1\text{Co}}$	16.67	-1.32
333-A- $\text{Ni}_{0\text{Ni}}^{3\text{Mn} - 3\text{Co}}$	16.67	-1.24
622-A- $\text{Ni}_{4\text{Ni}}^{2\text{Mn} - 0\text{Co}}$	16.67	-0.88
622-A- $\text{Ni}_{2\text{Ni}}^{2\text{Mn} - 2\text{Co}}$	16.67	-0.04
811-A- $\text{Co}_{4\text{Ni}}^{2\text{Mn}}$	11.11	-2.19
811-B- $\text{Co}_{6\text{Ni}}^{0\text{Mn}}$	11.11	-1.51
333-A- $\text{Co}_{3\text{Ni}}^{3\text{Mn}}$	11.11	-1.39
622-A- $\text{Co}_{5\text{Ni}}^{1\text{Mn}}$	16.67	0.10
333-A- $\text{Co}_{3\text{Ni}}^{3\text{Mn}}$	16.67	-0.16
811-A- $\text{Mn}_{4\text{Ni}}^{2\text{Co}}$	11.11	-1.46
811-B- $\text{Mn}_{6\text{Ni}}^{0\text{Co}}$	11.11	-1.43
333-A- $\text{Mn}_{3\text{Ni}}^{3\text{Co}}$	11.11	-0.57
622-A- $\text{Mn}_{5\text{Ni}}^{1\text{Co}}$	16.67	0.46
333-A- $\text{Mn}_{3\text{Ni}}^{3\text{Co}}$	16.67	0.97

Turning our attention to metal specific trends, we find that nickel release (at 11.11% surface vacancy) tracks as a function of the number of cobalt neighbors across both the 811 and 333

surfaces. The more cobalt neighbors about nickel, the more tightly they hold onto nickel. At 16.67%, both nickel release values are still negative, but smaller in size, and within 0.1 eV of each other. This indicates that at the higher surface vacancy concentration, compositions with 33-66% nickel may exhibit similar nickel release. To illustrate this, we calculate the maximum differences in  $\Delta G_{\text{diss}}$  for each surface vacancy concentration. For 11.11% nickel surface vacancies, for compositions that started with 78 or 33% nickel, this number is 0.80 eV. At 16.67% nickel surface vacancy density, for compositions with 66 or 33% nickel, it is 0.08 eV, or one-tenth the value at lower vacancy density. For cobalt and manganese release at 11.11% surface vacancy density, these numbers are 0.80 and 0.89 eV, respectively, and release at 16.67% is predicted to be thermodynamically unfavorable. The variation in  $\Delta G_{\text{diss}}$  across all compositions at 11.11% surface vacancy density is similar, meaning that the Ni>Co>Mn trend in release is upheld at lower surface vacancy densities, but as the metals are released, only nickel is predicted to continue release beyond 16.67%. The thermodynamics of metal release follow the previously observed incongruent dissolution.<sup>38,40</sup>

While the two media used in this study have different compositions, they both have similar, slightly alkaline pHs. However, the pH-dependent release of transition metals from NMC was investigated to provide insight about how aqueous conditions affect cation release. In general, we find that for the nickel, manganese, and cobalt pH-dependent release profiles in Figure 3,  $\Delta G_{\text{diss}}$  values track as Ni>Co>Mn, and that  $\Delta G_{\text{diss}}$  of 1/9 transition metal release (11.11% surface vacancy density) is more negative than for 1/6 transition metal release (16.67%). In these plots, the dotted black line indicates  $\Delta G_{\text{diss}}=0$ , as release is predicted to be thermodynamically unfavorable for  $\Delta G>0$ . We compute that for almost all removed transition metals,  $\Delta G_{\text{diss}}$  of the Ni-enriched NMC are lower than for equ stoichiometric NMC, which are shown as the dashed lines in Figure 3. This is caused by increasing the amount of nickel from 33 to 66 or 78%, relative to the amount of manganese and cobalt; in Ni-enriched NMC configurations, there is an interruption of the cation identity and oxidation states that are found

in the perfectly alternating NMC 333 configurations. The perturbations to chemical environment, via changing the identity of the neighboring cations, is most evident for  $\Delta G_{\text{diss}}$  values corresponding to 1/9 transition metal release. All solid lines (corresponding to 1/9 transition metal release) in Figure 3 are lower than the dashed lines for 333 NMC. In these plots, nickel and cobalt display large variations in  $\Delta G_{\text{diss}}$ , pointing towards a dependence of chemical environment on metal release, while manganese seems insensitive. The  $\Delta G_{\text{diss}}$  vs. pH plot for manganese shows two lines that almost overlap, while for nickel and cobalt, there are multiple solid lines with different  $\Delta G_{\text{diss}}$  at the same pH.

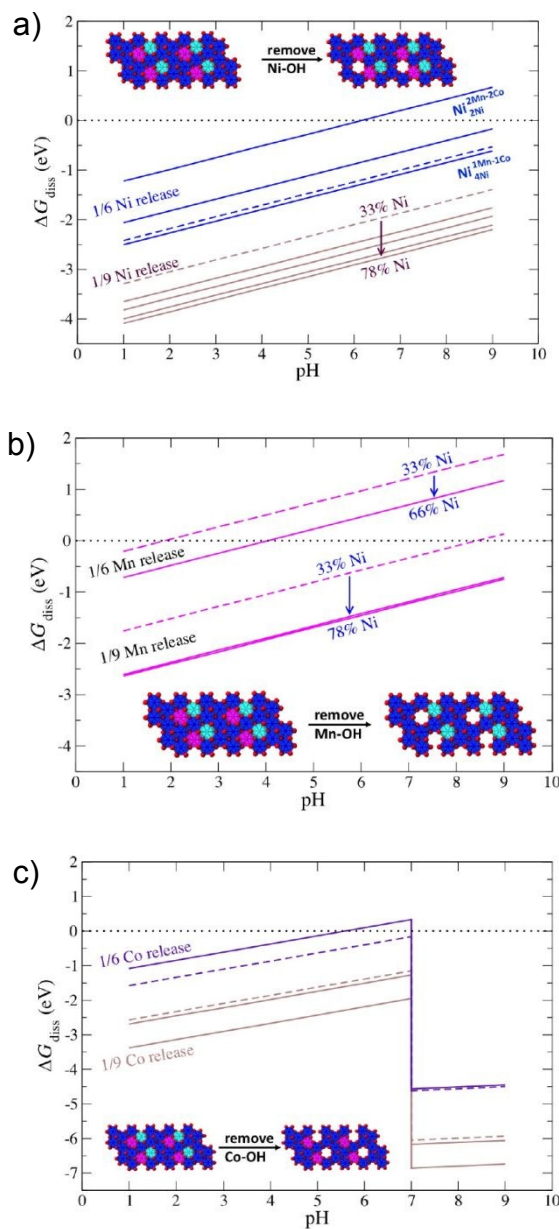
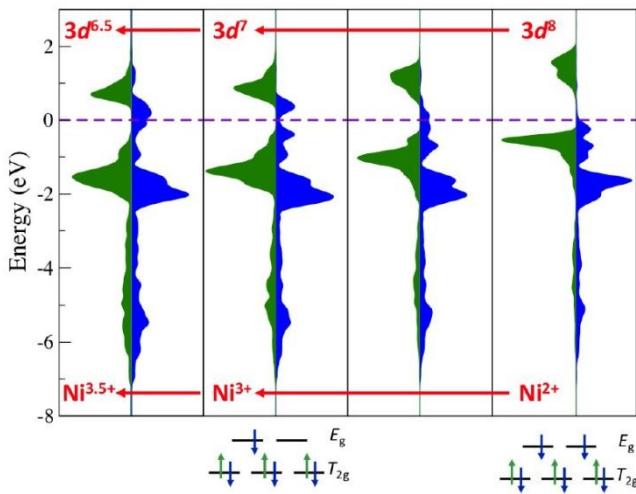


Figure 3. Theoretical calculations compute the release of ions from NMC. pH-dependent release profiles of a) nickel, b) manganese, and c) cobalt from NMC supercell surface slabs. Dashed lines refer to cation release from the equi-stoichiometric 333 NMC and solid lines refer to cation release from Ni-enriched NMC compositions. The dotted black line indicates  $\Delta G_{\text{diss}}=0$ .

There are three exceptions to  $\Delta G_{\text{diss}}$  of the Ni-enriched NMC being lower than for equi-stoichiometric NMC, and they all occur for 1/6 transition metal release. The specific cations are 622-A- $\text{Ni}_{2\text{Ni}}^{2\text{Mn}-2\text{Co}}$ , 622-A- $\text{Ni}_{4\text{Ni}}^{1\text{Mn}-1\text{Co}}$ , and 622-A- $\text{Co}_{5\text{Ni}}^{1\text{Mn}}$ , which have at least 1/3 nickel

neighbors. One reason for the switch in transition metal release trend for these cations could be that before removal, the nickel behaves more like a  $\text{Ni}^{4+}$  than  $\text{Ni}^{2+}$ , and that 622-A- $\text{Co}_{5\text{Ni}}^{1\text{Mn}}$  is one of its neighbors. Release of any transition metal with a 4+ oxidation state will be less energetically favorable than for a transition metal in the 2+ oxidation state, because the aqueous stable transition metal species are all 2+, and higher oxidation states (3+, 4+) will require a reduction step to be released in solution as aqueous cations.

The DFT total charge density is decomposed into atomic contributions using a projected density of states (PDOS) analysis. The PDOS of the 622-A surface slab shows that nickel exists in a range of oxidation states, and we find that the range of oxidation states can be correlated to the ease of metal release. Figure 4 is the PDOS of surface nickel and can be used as a guide to determine the redox properties of specific nickel. For all four surface nickel PDOS, the spin up peaks, shown as green curves both above and below the Fermi level ( $E_F$ , dashed line) remain almost constant. The spin down peaks, blue curves, evolve as a function of oxidation state. On the far right, they are found only below  $E_F$ , consistent with a  $3d^8 \text{Ni}^{2+}$  cation. As one goes from right to left, the blue peaks cross  $E_F$ , indicating an increase in oxidation state as nickel loses electrons in the filled spin down state. The crystal field split diagrams at the bottom of Figure 4 are color coded to illustrate the differences in spin population of surface nickel in Ni-enriched NMC for  $\text{Ni}^{2+}$  and  $\text{Ni}^{3+}$ . The highest oxidation state observed is on the far left, where nickel is trying to oxidize further to become a  $\text{Ni}^{4+}$ . A consequence of the range of oxidation states found in Ni-enriched NMC is that the surface states will be metallic.



**Figure 4. PDOS of surface nickel in the 622-A supercell surface slabs shows distinct nickel oxidation states. Nickel species are, from left to right,  $\text{Ni}_2\text{Mn} - 2\text{Co}$ ,  $\text{Ni}_2\text{Mn} - 0\text{Co}$ ,  $\text{Ni}_4\text{Mn} - 0\text{Co}$ , and  $\text{Ni}_4\text{Mn} - 1\text{Co}$ . Spin-up electrons are green, spin-down electrons are blue, and the Fermi level ( $E_F$ ) is a dashed purple line set to 0 eV. Crystal field split diagrams are used to illustrate how the PDOS can be used to assign nickel oxidation states.**

These theoretical insights correlate well with what is seen in our experimental dissolution studies. Ion dissolution was measured in bacterial medium after 3 hours by removing NMC and then running ICP-MS analysis on the supernatant. As predicted by the calculations of  $\Delta G_{\text{diss}}$ , these materials exhibited a transition metal release rate trend of  $\text{Ni} > \text{Co} > \text{Mn}$  (Table 2). Even though 622 NMC has double the nickel content of 333 NMC, only a slightly higher nickel release by 622 NMC (44.3  $\mu\text{M}$  vs. 37  $\mu\text{M}$  for the highest NMC dose) is observed. This experimentally observed increased stability of the material corroborates with the increased stability imparted by nickel being in a higher oxidation state in Ni-enriched NMC that was predicted by theoretical calculations. A reduction in cobalt release was observed in 622 NMC (11.02  $\mu\text{M}$  vs. 19.1  $\mu\text{M}$  for the highest NMC dose) compared to 333 NMC. Given that nickel and cobalt have been identified as major players in NMC toxicity,<sup>38</sup> it is worth noting that the sum of released nickel and cobalt is essentially the same for 333 and 622 NMC. Both 333 and 622 NMC released similar concentrations of manganese after 3 h, which for the highest NMC dose were 8.5  $\mu\text{M}$  and 6.52  $\mu\text{M}$  manganese, respectively.

1  
2  
3 **Table 2. Release of ionic species from NMC nanoparticles into bacterial medium. ICP-MS analysis reveals the**  
4 **release of lithium, nickel, manganese, and cobalt from 333 and 622 NMC nanosheets after 3 hours in bacterial**  
5 **medium. The error represents the standard deviations from three analytical replicates collected for each**  
6 **condition.**

[NMC] (ppb)	NMC type							
	333				622			
	Li (μM)	Mn (μM)	Co (μM)	Ni (μM)	Li (μM)	Mn (μM)	Co (μM)	Ni (μM)
25	100 ± 3	8.5 ± 0.4	19.1 ± 0.7	37 ± 2	57 ± 2	6.52 ± 0.03	11.02 ± 0.05	44.3 ± 0.3
12.5	50 ± 2	5.4 ± 0.1	10.7 ± 0.2	19.9 ± 0.1	29 ± 1	5 ± 1	6.1 ± 0.2	24.0 ± 0.9
6	25 ± 3	3.1 ± 0.2	5.6 ± 0.2	10 ± 1	14.4 ± 0.8	2.2 ± 0.1	3.2 ± 0.2	12 ± 1
3	12.7 ± 0.7	1.74 ± 0.09	3.0 ± 0.2	5.2 ± 0.5	7.9 ± 0.9	1.2 ± 0.3	1.5 ± 0.3	6 ± 1
1.5	6.5 ± 0.7	0.99 ± 0.04	1.59 ± 0.09	2.7 ± 0.2	4.43 ± 0.07	0.7 ± 0.2	0.8 ± 0.2	4 ± 2

21  
22 A difference between the bacterial medium used here and the daphnid medium is the presence  
23 of the organic component, sodium lactate. To understand the effects of the presence of this  
24 organic acid on NMC dissolution, the dissolution was determined in bacterial medium with and  
25 without lactate. Small organic acids have been shown to enhance dissolution of NMC materials,  
26 a phenomenon which is being harnessed by the recycling community.<sup>42–44</sup> In this work, it was  
27 noted that the presence of lactate in the bacterial medium did cause increased dissolution of the  
28 transition metal components of NMC (Figure 5). The data for the other transition metals are not  
29 plotted, as the dissolution of manganese and cobalt in bacterial medium without lactate was  
30 below the detection limit of the ICP-MS. However, in bacterial medium with lactate, detectable  
31 quantities of both metals were measured.  
32  
33  
34  
35  
36  
37  
38  
39  
40  
41  
42  
43  
44  
45  
46  
47  
48  
49  
50  
51  
52  
53  
54  
55  
56  
57  
58  
59  
60

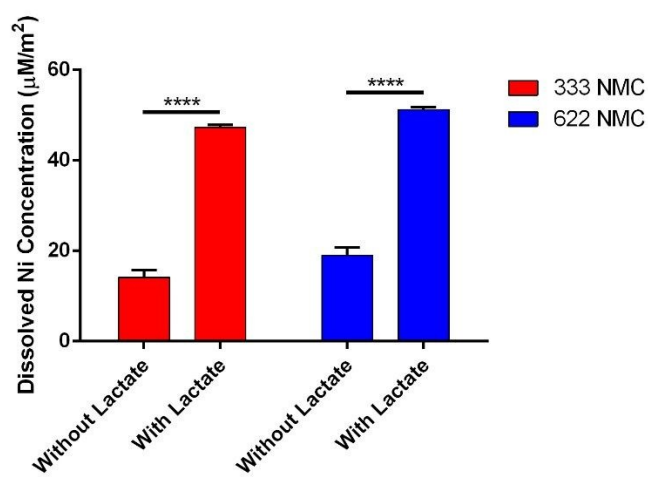


**Figure 5. Dissolution of nickel from 333 and 622 NMC was normalized by the surface area of the material. These data show that the presence of lactate causes increased nickel dissolution in both NMC types. Statistical testing was done using a two-way ANOVA with Sidak's multiple comparisons test. \*\*\*\*p<0.0001**

Computational modeling was also completed to understand the differences in energetics of dissolution for 333 NMC in bacterial medium in the presence and absence of lactate. Visual MINTEQ analysis results for 333 NMC in bacterial medium suggest that the relevant ligated metal forms are mono- and bi-lactate, and we limit calculations of  $\Delta G_3$  to these forms. All the bi-lactate ligated complexes are the *trans* isomer as our calculations have determined for these isomers to be more stable than *cis* isomers. For nickel, manganese, and cobalt, the  $\Delta G_3$  values are tabulated below (Table 3).

**Table 3. The values of  $\Delta G_3$  for reactions (1) and (2).**

	eV	Co <sup>2+</sup>	Ni <sup>2+</sup>	Mn <sup>2+</sup>
$\Delta G_3$ [1LA]	-0.95	-0.61	-0.51	
$\Delta G_3$ [2LA]	-1.37	-0.96	-1.01	

Given that overall  $\Delta G_{diss}$  is the sum over  $\Delta G_1$ ,  $\Delta G_2$  and  $\Delta G_3$ , the favorable values of  $\Delta G_3$  can be interpreted as a measure of lactate chelation as a thermodynamic driving force for (more) favorable metal release. For cobalt (nickel),  $\Delta G_3$  to form the bi-lactate complex is 0.42 (0.35) eV more favorable than for the mono-lactate complex. The MINTEQ analysis shows the percentages of mono- and bi-lactate to be 42% versus 36% for cobalt, and 41% versus 43% for nickel, thus the results of  $\Delta G_3$  align better with the MINTEQ results for nickel. However, we note

that the  $\Delta G_3$  calculations do not take into account all ions in solution, and consider the trends in  $\Delta G_3$  for the two forms to be in reasonable agreement with the relative amounts from the MINTEQ analysis. For manganese, the MINTEQ results suggest that the hydrated cation is the dominant speciation in bacterial medium. While  $\Delta G_3$  values for manganese are negative, we note that unlike nickel and cobalt, the value of  $\Delta G_{SHE}^0$  is larger in magnitude:  $\Delta G_{SHE}^0 = -0.563$  eV (Co<sup>2+</sup>), -0.472 eV (Ni<sup>2+</sup>), and -2.363 eV (Mn<sup>2+</sup>). This suggests a weak thermodynamic driving force for Mn<sup>2+</sup> to continue to react to form ligated complexes relative to Co<sup>2+</sup> and Ni<sup>2+</sup>, which helps to interpret the experimental results of the study. This is the first instance using the DFT + solvent ion model for cation release that goes on to include additional aqueous chemical reactions (like metal complex formation with lactate examined here) to help interpret metal specific trends in dissolution in different aqueous media.

#### 4.4 Toxicity of Released Ions from NMC Nanoparticles to *S. oneidensis*

To assess the toxicity of the ions that are released over the course of bacterial exposure to NMC, the bacteria were exposed to the same concentration of ions as determined by ICP-MS for 3 h, and viability was again measured using a growth-based viability assay. Toxicity from the released ions recapitulated the toxicity observed with the nanoparticles themselves for the bacteria (Figure 6). This implicates the ions as a major source of toxicity of the nanoparticles to bacterial species, which is consistent with previous work.<sup>38</sup> Given that the total concentration of nickel and cobalt released from 333 and 622 NMC was similar, this also suggests that the two ions have an equal role in the toxicity of the material to *S. oneidensis*. Nickel and cobalt toxicity to organisms is mainly due to their ability to either generate reactive oxygen species or to interfere with important enzymes via several mechanisms,<sup>45,46</sup> and both of these could be contributing factors to the observed toxicity. Taken together with the increased material stability demonstrated by our theoretical and experimental approach, these findings shed light on the unexpected toxicity results obtained which showed equal toxicity from 333 NMC and 622 NMC. Since dissolution of the materials are essentially equivalent, and ions appear to dominate the

1  
2  
3  
4  
5  
6  
7  
8  
9  
10  
11  
12  
13  
14  
15  
16  
17  
18  
19  
20  
21  
22  
23  
24  
25  
26  
27  
28  
29  
30  
31  
32  
33  
34  
35  
36  
37  
38  
39  
40  
41  
42  
43  
44  
45  
46  
47  
48  
49  
50  
51  
52  
53  
54  
55  
56  
57  
58  
59  
60

toxicity to bacteria here, this explains why 333 NMC and nickel-enriched NMC compositions exhibit equivalent toxicities to *S. oneidensis*. Therefore, we rule out the possibility that there are other novel mechanisms at play that contribute to the bacterial toxicity of nickel-enriched NMC materials.

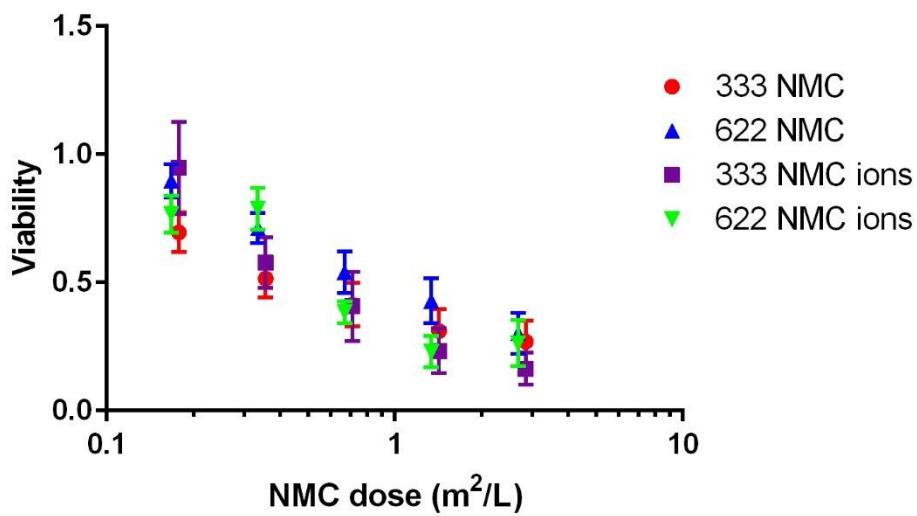


Figure 6. The toxicity from the ions that are released from NMC recapitulate the toxicity observed for the respective nanoparticle to *S. oneidensis*. Please note that the toxicity data for 333 NMC and 622 NMC here is the same as from Figure 2 and is included to facilitate interpretation. The error bars indicate the standard error from seven replicates for the NMC materials and four replicates for the ion controls.

#### 4.5 Abiotic ROS Production from NMC Nanoparticles in Bacterial Medium

To investigate the production of NMC-induced ROS from the NMC nanomaterials, different dyes were used as reporters of ROS levels after 3 h exposure. To detect overall ROS levels, H<sub>2</sub>DCF-DA was used, and to detect hydroxyl radical specifically, APF was used. The level of ROS production from the commercial materials could not be determined since at matching surface area doses, the concentrations were so high that fluorescence from the dyes would be masked by the turbidity of the suspensions.

It is seen that 622 NMC generates more hydroxyl radicals in bacterial medium, but significant hydroxyl radical generation does not occur with 333 NMC (Figure 7). Given that a majority of the added nickel in Ni-enriched NMC was in an oxidation state higher than +2 and

1  
2  
3 that dissolution of the transition metals from NMC that are not already at their lowest oxidation  
4 state ( $\text{Ni}^{2+}$ ,  $\text{Mn}^{2+}$ , and  $\text{Co}^{2+}$ ) need to initiate an oxidative reaction that produces ROS to  
5 dissolve,<sup>22,40</sup> it was expected that Ni-enriched NMC would produce more hydroxyl radicals. It  
6 was noted that the overall production of ROS by 333 and 622 NMC is at significant levels  
7 compared to a NP-free control. While identifying the ROS species being generated by these  
8 materials is outside the scope of this work, this will be the focus of future studies. In bacterial  
9 medium, 333 NMC is producing more ROS than 622 NMC (normalized fluorescence of 0.90 vs  
10 0.83, respectively). While overall production of ROS by 333 NMC is greater in bacterial medium,  
11 it is noted that there is significantly greater generation of hydroxyl radical, a very highly reactive  
12 ROS with a half-life on the order of  $10^{-9}$  s,<sup>47</sup> by 622 NMC. From the observed APF fluorescence,  
13 it is likely that the amount of hydroxyl radicals generated by these materials is low. However, the  
14 interplay of the different ROS generated from these materials could be contributing to the equal  
15 toxicity seen by 333 and 622 NMC to *S. oneidensis*. This demonstrates that there is merit to  
16 further investigating the production of ROS by these materials to elucidate the contribution of  
17 ROS production to the overall toxicity of NMC; this work is currently underway.

18  
19  
20  
21  
22  
23  
24  
25  
26  
27  
28  
29  
30  
31  
32  
33  
34  
35  
36  
37  
38  
39  
40  
41  
42  
43  
44  
45  
46  
47  
48  
49  
50  
51  
52  
53  
54  
55  
56  
57  
58  
59  
60

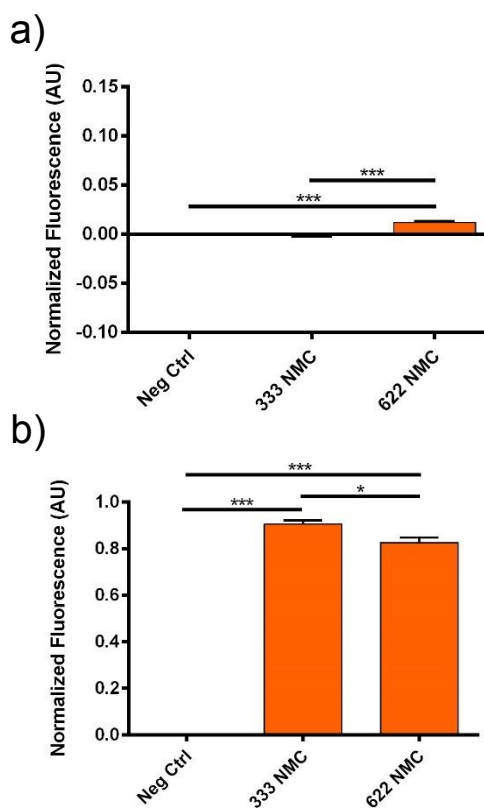


Figure 7. Abiotic ROS generation from NMC nanoparticles in bacterial medium. Fluorescent dyes were used to assess the production of a) hydroxyl radicals from NMC nanoparticles, which shows that 622 NMC produces more ·OH than 333 NMC. Monitoring b) general production of ROS reveals that 333 NMC is producing more ROS than 622 NMC. The fluorescent intensities were background subtracted and normalized to the positive control; statistical analysis was done with a one-way ANOVA. \*p<0.05, \*\*\*p<0.001

#### 4.6 NMC Association to *S. oneidensis*

To determine whether there is any direct interaction of NMC materials with *S. oneidensis*, following NMC exposure, TEM micrographs and hyperspectral images were acquired to give visual evidence of material association (Figure 8). From the TEM images, instances of binding of 333 and 622 NMC to *S. oneidensis* MR-1 can be seen, but it is not very frequent. Analysis of the hyperspectral images, however, shows more instances of binding of the nanoparticles to bacteria than the TEM images. A spectral library was created for the bacteria and the NMC materials; in the hyperspectral images, any pixel where these signals were identified are falsely colored red or green, respectively. It is apparent that there is significant binding observed for

these materials as colocalization of these colors can be seen for both the nanoparticles as well as the commercial, microscale materials. With the microscale materials, it appears as though the bacteria swarm the larger chunks, while small chunks are bound to their surface similarly to the nanoscale chunks of 333 and 622 NMC (Figure S8). This is the first instance showing significant binding between NMC materials and *S. oneidensis*. Given that minimal binding is seen in the TEM images, this suggests that the interaction between *S. oneidensis* and NMC is a weak binding interaction, as the centrifugation steps for biological TEM prep are likely removing the nanoparticles from the bacterial surface, which is why these interactions have not previously been observed. Binding of nanoparticles to bacterial surfaces can help to facilitate toxicity by disrupting the cell wall,<sup>48–50</sup> initiating internal pathways within the cell,<sup>51</sup> by dissolving toxic ions right at the cell surface,<sup>52</sup> or by generating ROS near the bacterial surface.<sup>53</sup> Given that it is known that ion dissolution is a major pathway for toxicity of these materials, NMC binding to the bacterial surface will facilitate the dissolution of ions near the bacteria. However, since the toxicity of ions alone recapitulates the toxicity of the nanoparticles, if there is any enhancement in toxicity due to nanoparticle binding to bacteria in this case, it is minute.

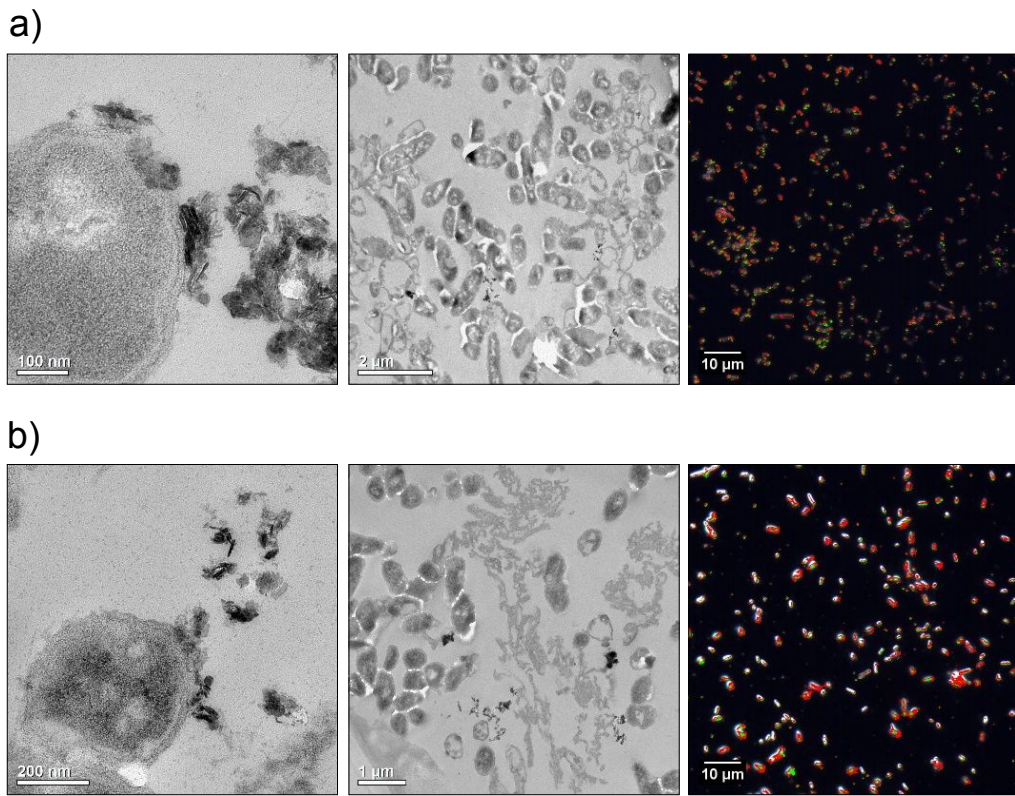


Figure 8. NMC association with *S. oneidensis*. The attachment of a) 333 NMC and b) 622 NMC to *S. oneidensis* was assessed using two imaging techniques. (Left column) Zoomed in TEM images showing interacting particles or those in close proximity to the cell surface, (middle column) zoomed out image showing the frequency of interaction, and (right column) hyperspectral image that has been falsely colored to show the colocalization of signals from bacteria (red) and NMC (green).

#### 4.7 Toxicity of NMC materials to *D. magna*

To increase the biological diversity in this study, as well as use an organism that occupies a different trophic level from *S. oneidensis*, the effects of NMC exposure on *D. magna* were also investigated. While the major toxicity mechanism of NMC to *S. oneidensis* is in its release of toxic ions, toxicity in *D. magna* has been shown to be nanoparticle-specific. To test the acute toxicity of nickel-enriched NMC, daphnids were exposed for 48 hours, and survival at 24 and 48 hours was assessed (Figure 9). For these materials, it can be seen that daphnid survival is significantly reduced for 333 NMC at 1.1 and 2.8  $\text{m}^2/\text{L}$  and for 622 NMC at 0.11, 1.1, and 2.7  $\text{m}^2/\text{L}$ . Given that a lower dose of 622 NMC is required to exhibit toxicity, these results indicate

that the 622 NMC is more toxic than 333 NMC to *D. magna*. While 622 NMC is toxic at all doses used here, a reduction in toxicity is seen in the highest dose applied, which is likely due to the increased aggregation observed in 622 NMC at this concentration.

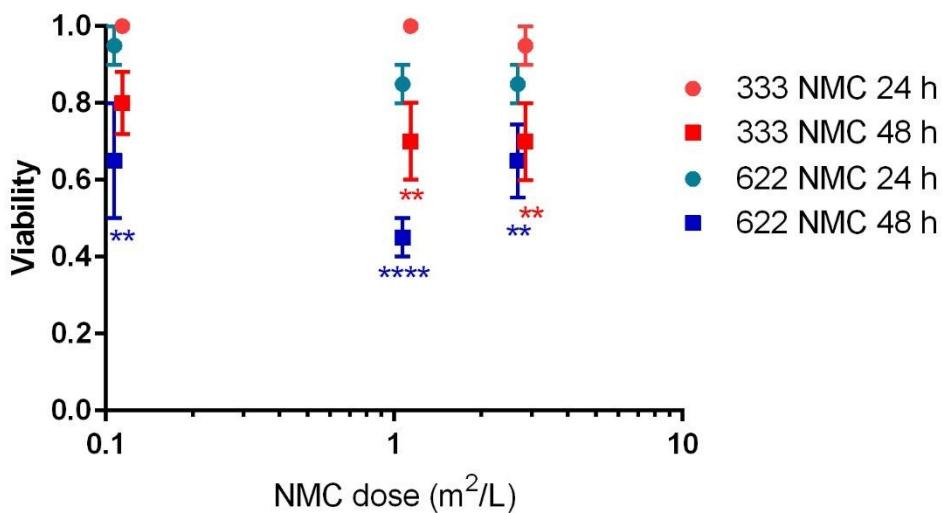


Figure 9. Assessment of daphnid survival after 24 and 48 hours of exposure to 333 NMC and 622 NMC. The error bars in these graphs represent the standard error from four exposure replicates. The error bars are not visible for the data points where all daphnids survived exposure. Two-way ANOVA was used to assess the statistical significance between each treatment and the negative control. \*\* $p<0.01$ , \*\*\*\* $p<0.0001$

In previous work, it was noted that the actual NPs have an impact on daphnids rather than the ion dissolution from the NPs, which explains why even though these materials have similar dissolution profiles, 622 NMC is exhibiting higher toxicity to *D. magna*. Furthermore, *D. magna* are more sensitive to nickel and cobalt than to manganese,<sup>54</sup> and it therefore makes sense that Ni-enriched NMC would be more toxic.

#### 4.8 Cation Release in Daphnid Medium

NMC dissolution in daphnid medium was checked similarly to the dissolution in bacterial medium, with the intention of informing ion controls. Since daphnid medium does not contain lactate, overall NMC dissolution was lower; however, the release trend of Ni>Co>Mn also holds true in daphnid medium. Also, the sum of the released toxic components, nickel and cobalt, is

generally the same. However, for the highest dose of NMC used, the sum of nickel and cobalt dissolution is higher for 622 NMC than for 333 NMC (Table 4).

**Table 4. Release of ionic species from NMC NPs into daphnid medium as revealed by ICP-MS. This shows the order of release from the transition metals is Ni>Co>Mn. The error arises from standard deviations of 3 analytical replicates.**

[NMC] (ppb)	NMC type							
	333				622			
	Li (μM)	Mn (μM)	Co (μM)	Ni (μM)	Li (μM)	Mn (μM)	Co (μM)	Ni (μM)
25	115 ± 3	0.03 ± 0.03	0.10 ± 0.03	1.7 ± 0.3	34 ± 2	-0.003 ± 0.001	0.007 ± 0.004	2.3 ± 0.4
10	44 ± 3	0.000 ± 0.002	0.17 ± 0.01	1.4 ± 0.1	13.0 ± 0.5	0.000 ± 0.006	0.016 ± 0.007	1.7 ± 0.2
1	4.2 ± 0.8	0.003 ± 0.002	0.101 ± 0.008	0.29 ± 0.04	1.258 ± 0.008	-0.001 ± 0.004	0.023 ± 0.002	0.31 ± 0.02

#### 4.9 Toxicity of Released Ions to Daphnids

To assess the toxicity of the ions released in daphnid medium over the 48 hour exposure, daphnids were exposed to the ions at the measured release concentrations for 48 hours. We observe higher concentrations of released ions in the bacterial medium than the daphnid medium, as previously reported.<sup>38,55</sup> The enhanced dissolution was due to the high concentration of lactate (100 mM) in the bacterial medium. As in previous work,<sup>55</sup> daphnids were unaffected by the bulk release of ions from the NMC nanoparticles used in this study (Figure 10), suggesting again that daphnids experience a NP-specific toxicity from NMC. The different dissolution behaviors of the materials in each media could also explain why there is a NP-specific toxicity for *D. magna*, as there is reduced ion dissolution in the daphnid medium.

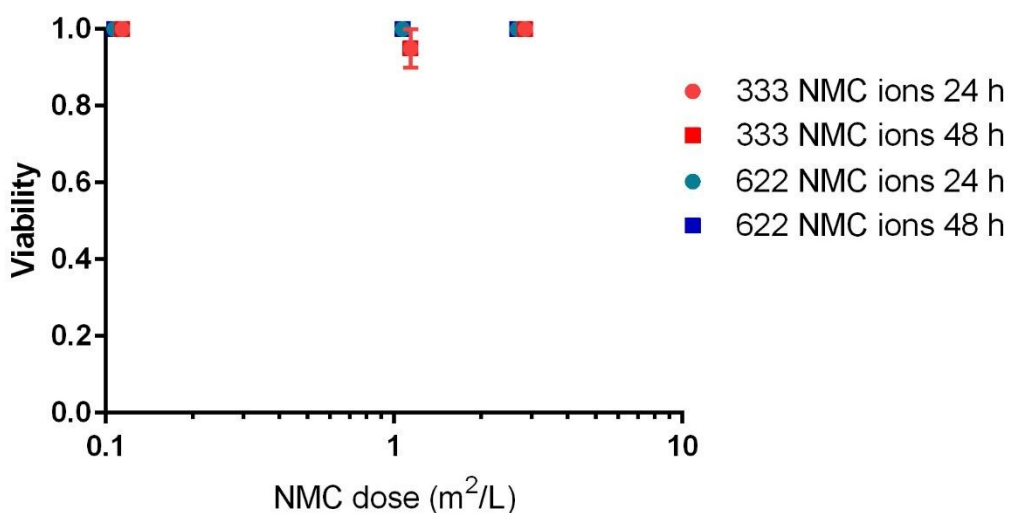


Figure 10. The toxicity of released ions from NMC nanoparticles to *D. magna* show that daphnids are tolerant of the ions released from both 333 NMC and 622 NMC over a 48 hour exposure. Since all of the daphnids survived the ion exposures (with the exception of the 1.1  $\text{m}^2/\text{L}$  ion equivalents from 333 NMC), all of the points are overlaid on each other at 100% daphnid survival. The error bars are from the standard error of triplicate exposures to sets of five animals. Some error bars are not visible due to all of the daphnids surviving the exposure.

#### 4.10 ROS Production from NMC in Daphnid Medium

The production of ROS from NMC was monitored in daphnid medium using two fluorescent-based dyes (Figure 11). In daphnid medium, it was observed that both nanoparticle types were producing significantly more ROS than the NP-free control. However, contrary to what was seen in bacterial medium, 622 NMC is producing more ROS than 333 NMC (normalized fluorescence of 0.73 vs 0.52, respectively) in daphnid medium; it is important to note that we observed that 622 NMC was also more toxic to *D. magna*. While it was not a statistically significant difference, there was also increased production of hydroxyl radicals from 622 NMC compared to 333 NMC. ROS induces toxicity to organisms in a variety of ways,<sup>53,56,57</sup> and the data from both media suggest that ROS could be contributing to the toxicity seen from these materials to both *S. oneidensis* and *D. magna*. Given that equal ROS production and toxicity was seen by both NMC materials in bacterial medium, but that in daphnid medium increased toxicity and increased ROS production was noted with 622 NMC, these preliminary findings demonstrate that the pattern of ROS production in each media matches the toxicity pattern seen with both organisms.

However, these do not implicate ROS production as a contributor to this toxicity mechanism, as these dyes can only show relative ROS production as opposed to giving absolute quantities, but they do point to the fact that future studies should be performed to more fully understand the role of ROS production in the toxicity of these materials.

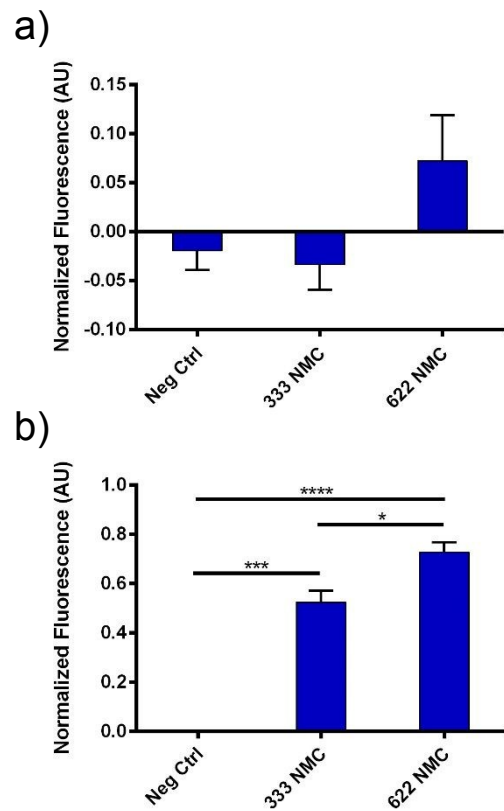
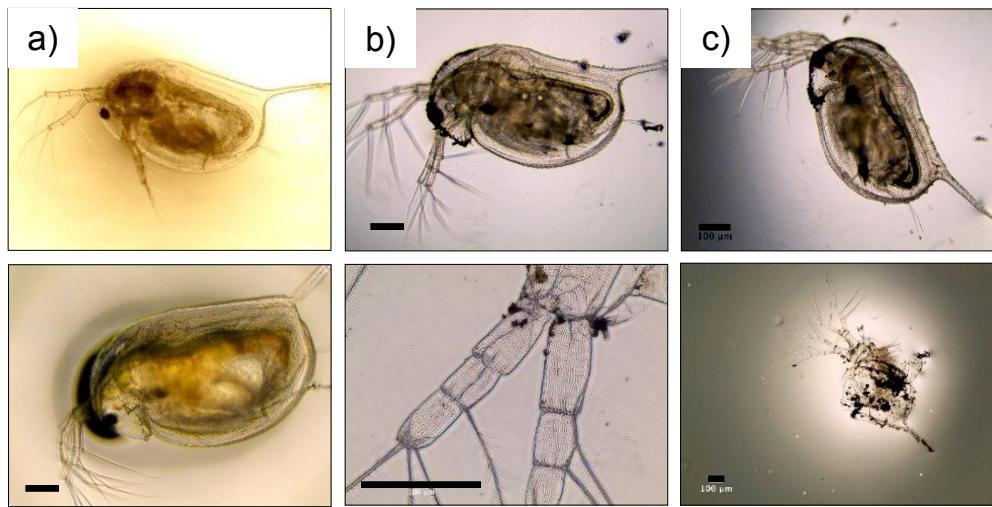


Figure 11. The production of a) hydroxyl radicals in daphnid medium was monitored using APF, which showed that, like in the bacterial medium, 622 NMC is producing more hydroxyl radical than 333 NMC, but the difference is not statistically significant. Assessment of b) overall ROS production using H<sub>2</sub>DCF-DA also demonstrates that there is increased production of ROS by 622 NMC than 333 NMC. The fluorescence intensities were background subtracted and normalized to the positive control. Statistical analysis was performed using a one-way ANOVA with Tukey's multiple comparisons test. \*p<0.05, \*\*\*p<0.001, \*\*\*\*p<0.0001

#### 4.11 Association of NMC to *D. magna*

To observe direct interaction with *D. magna*, brightfield microscopy was used. From the images collected, interaction of *D. magna* with all of the NMC materials can be seen (Figure 12). It can be seen for these nanoparticles that they are mostly adhering to the daphnid carapace. This could negatively impact the daphnids by disrupting the membrane or being taken up intracellularly via different processes, releasing ions right at the daphnid surface, or by causing

the daphnids to molt more frequently (a defense mechanism for daphnids to remove metal pollutants<sup>58</sup>) and thus use more energy. Given the overall greater production of ROS by 622 NMC in daphnid medium, ROS generation at the surface of the animal may also be contributing to the toxicity (the contribution of which needs to be investigated further), which would be enhanced by the greater binding observed by 622 NMC than 333 NMC.



**Figure 12. NMC association with *D. magna*.** Microscope images of *D. magna* after 48 hour exposure to NMC or to a) no NMC materials. Images of live daphnids after exposure to b) 333 NMC nanosheets and c) 622 NMC nanosheets shows NMC association both with the exterior of the animal, which can be seen in the zoomed in images (bottom row) and in the gut. All of the scale bars indicate 100  $\mu$ m.

## 5. Conclusions

The data presented here demonstrate that redesign of NMC to a nickel-enriched composition has differential impacts on bacteria and daphnids, and this could be due to different mechanisms at work. The Ni-enriched material has the same impact on our bacterial model as equ stoichiometric NMC when exposed at matching surface areas, due to equivalent ion dissolution from the materials. Given that nickel is a toxic component of the material, this was a surprising result. However, to the authors' knowledge, the computational work in this study is the first instance that it was demonstrated that there is increased stability of the NMC material against dissolution due to the oxidation states of the additional nickel in Ni-enriched NMC. These calculations indicated that this increased stability meant that similar dissolution of toxic ions would be noted for both 333 and 622 NMC. Indeed, similar dissolution profiles between 333

1  
2  
3 and 622 NMC were obtained in experiments, and since *S. oneidensis* is known to be sensitive  
4 to ion release, this explains why, although an unexpected result, we saw similar toxicities  
5 between the two materials to *S. oneidensis*. For the invertebrate, *D. magna*, 622 NMC was  
6 found to be more toxic than equ stoichiometric NMC and no impact was found related to ion  
7 dissolution from the materials. The pattern of ROS production by NMC mirrored the toxicity seen  
8 in the two media, suggesting that ROS production could be contributing to the overall toxicity of  
9 the material, and further experiments are underway to understand the role of ROS production in  
10 the toxicity of these materials. For *D. magna*, the toxicity is dictated by the core composition of  
11 the material, and since nickel is more toxic than manganese to these organisms, doping in extra  
12 nickel at the expense of manganese leads to a negative impact. This is a significant  
13 observation, and reveals the importance of determining the molecular mechanisms of toxicity to  
14 organisms to inform redesign efforts. This work also demonstrates a method to evaluate a  
15 nanoparticle redesign strategy using a computational front when the toxicity mechanism is  
16 known.

## 6. Acknowledgements

1  
2  
3 This work was supported by the National Science Foundation under the Center for Sustainable  
4 Nanotechnology, CHE-1503408. The CSN is part of the Centers for Chemical Innovation  
5 Program. J.T.B. was supported by a National Science Foundation Graduate Research  
6 Fellowship (grant number 00039202). TEM imaging in this study was carried out in the  
7 Characterization Facility, University of Minnesota, which receives partial support from the  
8 National Science Foundation through the MRSEC program. The authors gratefully acknowledge  
9 Fang Zhou at the Characterization Facility for microtome preparation of resin-embedded  
10 samples for TEM. The authors thank Elizabeth Lundstrom for ICP-MS analysis of the ion  
11 dissolution samples in bacterial medium as part of the University of Minnesota Earth Sciences  
12 Department. The authors acknowledge the Trace Element Research Group at the UW-Madison,  
13 Wisconsin State Laboratory of Hygiene (WSLH) for their analytical services (magnetic-sector

1  
2  
3 ICPMS) for the ion dissolution samples in daphnid medium. The authors are thankful to Tianlei  
4 Yan for his contributions to NMC synthesis. This research was supported in part through  
5 computational resources provided by the University of Iowa, Iowa City, Iowa. This work used the  
6 Extreme Science and Engineering Discovery Environment (XSEDE<sup>59</sup>), which is supported by  
7 National Science Foundation grant number ACI-1548562 through allocation ID TG-GEO160006.  
8  
9

10 **Corresponding author:**

11 Prof. Christy Haynes, University of Minnesota, chaynes@umn.edu  
12  
13

14 **ORCID IDs of Authors:**

15 Joseph T. Buchman: 0000-0001-5827-8513  
16  
17

18 Evan A. Bennett:  
19  
20

21 Chenyu Wang:  
22  
23

24 Ali Abbaspour Tamijani:  
25  
26

27 Joseph W. Bennett: 0000-0002-7971-4772  
28  
29

30 Blake G. Hudson:  
31  
32

33 Curtis M. Green: 0000-0001-7236-7408  
34  
35

36 Peter L. Clement: 0000-0003-2959-7253  
37  
38

39 Bo Zhi: 0000-0002-1918-5012  
40  
41

42 Austin H Henke:  
43  
44

45 Elizabeth D. Laudadio: 0000-0002-3522-1722  
46  
47

48 Sara E. Mason: 0000-0003-1515-6780  
49  
50

51 Robert J. Hamers: 0000-0003-3821-9625  
52  
53

54 Rebecca D. Klaper: 0000-0002-9239-6916  
55  
56

57 Christy L. Haynes: 0000-0002-5420-5867  
58  
59

1  
2  
3 **7. Electronic Supplemental Information.** Additional materials used; surface area  
4 determination of commercial NMC, stoichiometry of c622 and c811 NMC from EDS; X-ray  
5 diffraction characterization of nanoscale NMC; transmission electron micrographs of NMC  
6 materials; scanning electron micrographs of nanoscale NMC; zeta potential of NMC in each  
7 media; Li-terminated and H-terminated surface models of Ni-enriched NMC; determination of  
8  $\Delta G$  values used for computational studies; impact of bacterial presence on dissolution of  
9 commercial NMC; commercial NMC toxicity to *S. oneidensis*; comparison of  $\Delta G_3$  values  
10 determined by PBE and B3LYP; association of commercial NMC to *S. oneidensis*; commercial  
11 NMC toxicity to *D. magna*; association of commercial NMC to *D. magna*.  
12  
13

## 8. References

- 1 J.-M. Tarascon and M. Armand, Issues and challenges facing rechargeable lithium  
2 batteries, *Nature*, 2001, **414**, 359–367.
- 3 M. S. Whittingham, Lithium batteries and cathode materials, *Chem. Rev.*, 2004, **104**,  
4 4271–4301.
- 5 K. Mizushima, P. C. Jones, P. J. Wiseman and J. B. Goodenough,  $\text{Li}_x\text{CoO}_2$  (0< $x$ ≤1): A  
6 new cathode material for batteries of high energy density, *Mater. Res. Bull.*, 1980, **15**,  
7 783–789.
- 8 N. Nitta, F. Wu, J. T. Lee and G. Yushin, Li-ion battery materials: present and future,  
9 *Mater. Today*, 2015, **18**, 252–264.
- 10 M. Jacoby, It's time to get serious about recycling Lithium-ion batteries, *Chem. Eng.*  
11 *News*.
- 12 E. A. Olivetti, G. Ceder, G. G. Gaustad and X. Fu, Lithium-ion battery supply chain  
13 considerations: analysis of potential bottlenecks in critical metals, *Joule*, 2017, **1**, 229–  
14 243.
- 15 M. Okubo, E. Hosono, J. Kim, M. Enomoto, N. Kojima, T. Kudo, H. Zhou and I. Honma,  
16 Nanosize effect on high-rate Li-ion intercalation in  $\text{LiCoO}_2$  electrode, *J. Am. Chem. Soc.*,  
17 18

1  
2  
3 2007, **129**, 7444–7452.

4  
5 8 P. Poizot, S. Laruelle, S. Grugeon, L. Dupont and J.-M. Tarascon, Nano-sized transition-  
6 metal oxides as negative-electrode materials for lithium-ion batteries, *Nature*, 2000, **407**,  
7 496–499.

8  
9 9 M. Jo, Y.-S. Hong, J. Choo and J. Cho, Effect of  $\text{LiCoO}_2$  cathode nanoparticle size on  
10 high rate performance for Li-ion batteries, *J. Electrochem. Soc.*, 2009, **156**, A430–A434.

11 R. Xu, L. S. de Vasconcelos, J. Shi, J. Li and K. Zhao, Disintegration of meatball  
12 electrodes for  $\text{LiNi}_x\text{Mn}_y\text{Co}_z\text{O}_2$  cathode materials, *Exp. Mech.*, 2018, **58**, 549–559.

13 F. H. Pavoni, L. E. Sita, C. S. dos Santos, S. P. da Silva, P. R. C. da Silva and J.  
14 Scarmínio,  $\text{LiCoO}_2$  particle size distribution as a function of the state of health of  
15 discarded cell phone batteries, *Powder Technol.*, 2018, **326**, 78–83.

16 S. Watanabe, M. Kinoshita, T. Hosokawa, K. Morigaki and K. Nakura, Capacity fading of  
17  $\text{LiAl}_y\text{Ni}_{1-x-y}\text{Co}_x\text{O}_2$  cathode for lithium-ion batteries during accelerated calendar and cycle  
18 life tests (effect of depth of discharge in charge-discharge cycling on the suppression of  
19 the micro-crack generation of  $\text{LiAl}_y\text{Ni}_{1-x-y}\text{Co}_x\text{O}_2$  particle), *J. Power Sources*, 2014, **260**,  
20 50–56.

21 I. Belharouak, Y.-K. Sun, J. Liu and K. Amine,  $\text{Li}(\text{Ni}_{1/3}\text{Co}_{1/3}\text{Mn}_{1/3})\text{O}_2$  as a suitable cathode  
22 for high power applications, *J. Power Sources*, 2003, **123**, 247–252.

23 C. S. Johnson, N. Li, C. Lefief, J. T. Vaughey and M. M. Thackeray, Synthesis,  
24 characterization and electrochemistry of lithium battery electrodes:  $x\text{Li}_2\text{MnO}_3 \cdot (1-x)\text{LiMn}_{0.333}\text{Ni}_{0.333}\text{Co}_{0.333}\text{O}_2$  ( $0 \leq x \leq 0.7$ ), *Chem. Mater.*, 2008, **20**, 6095–6106.

25 J. B. Goodenough and Y. Kim, Challenges for rechargeable Li batteries, *Chem. Mater.*,  
26 2010, **22**, 587–603.

27 S. K. Martha, H. Sclar, Z. S. Framowitz, D. Kovacheva, N. Saliyski, Y. Gofer, P. Sharon,  
28 E. Golik, B. Markovsky and D. Aurbach, A comparative study of electrodes comprising  
29 nanometric and submicron particles of  $\text{LiNi}_{0.50}\text{Mn}_{0.50}\text{O}_2$ ,  $\text{LiNi}_{0.33}\text{Mn}_{0.33}\text{Co}_{0.33}\text{O}_2$ , and  
30

1  
2  
3 LiNi<sub>0.40</sub>Mn<sub>0.40</sub>Co<sub>0.20</sub>O<sub>2</sub> layered compounds, *J. Power Sources*, 2009, **189**, 248–255.  
4  
5 17 L. Ma, M. Nie, J. Xia and J. R. Dahn, A systematic study on the reactivity of different  
6  
7 grades of charged Li[Ni<sub>x</sub>Mn<sub>y</sub>Co<sub>z</sub>]O<sub>2</sub> with electrolyte at elevated temperatures using  
8  
9 accelerating rate calorimetry, *J. Power Sources*, 2016, **327**, 145–150.  
10  
11 18 W. Liu, P. Oh, X. Liu, M.-J. Lee, W. Cho, S. Chae, Y. Kim and J. Cho, Nickel-rich layered  
12  
13 lithium transition-metal oxide for high-energy lithium-ion batteries, *Angew. Chemie Int.*  
14  
15 *Ed.*, 2015, **54**, 4440–4457.  
16  
17 19 J. B. Dunn, L. Gaines, J. C. Kelly, C. James and K. G. Gallagher, The significance of Li-  
18  
19 ion batteries in electric vehicle life-cycle energy and emissions and recycling's role in its  
20  
21 reduction, *Energy Environ. Sci.*, 2015, **8**, 158–168.  
22  
23 20 H. H. Hau and J. A. Gralnick, Ecology and biotechnology of the genus *Shewanella*, *Annu.*  
24  
25 *Rev. Microbiol.*, 2007, **61**, 237–258.  
26  
27 21 R. D. Gulati, The ecology of common planktonic crustacea of the freshwaters in the  
28  
29 Netherlands, *Hydrobiologia*, 1978, **59**, 101–112.  
30  
31 22 J. W. Bennett, D. Jones, X. Huang, R. J. Hamers and S. E. Mason, Dissolution of  
32  
33 complex metal oxides from first-principles and thermodynamics: cation removal from the  
34  
35 (001) surface of Li(Ni<sub>1/3</sub>Mn<sub>1/3</sub>Co<sub>1/3</sub>)O<sub>2</sub>, *Environ. Sci. Technol.*, 2018, **52**, 5792–5802.  
36  
37 23 X. Rong and A. M. Kolpak, Ab initio approach for prediction of oxide surface structure,  
38  
39 stoichiometry, and electrocatalytic activity in aqueous solution, *J. Phys. Chem. Lett.*,  
40  
41 2015, **6**, 1785–1789.  
42  
43 24 T. A. Qiu, T. H. T. Nguyen, N. V. Hudson-Smith, P. L. Clement, D.-C. Forester, H. Frew,  
44  
45 M. N. Hang, C. J. Murphy, R. J. Hamers, Z. V. Feng and C. L. Haynes, Growth-based  
46  
47 bacterial viability assay for interference-free and high-throughput toxicity screening of  
48  
49 nanomaterials, *Anal. Chem.*, 2017, **89**, 2057–2064.  
50  
51 25 P. Hohenberg and W. Kohn, Inhomogeneous Electron Gas, *Phys. Rev.*, 1964, **136**,  
52  
53 B864–B871.  
54  
55  
56  
57  
58  
59  
60

1  
2  
3 26 W. Kohn and L. J. Sham, Self-consistent equations including exchange and correlation  
4 effects, *Phys. Rev.*, 1965, **140**, A1133–A1138.  
5  
6 27 P. Giannozzi, S. Baroni, N. Bonini, M. Calandra, R. Car, C. Cavazzoni, D. Ceresoli, G. L.  
7 Chiarotti, M. Cococcioni, I. Dabo, A. Dal Corso, S. de Gironcoli, S. Fabris, G. Fratesi, R.  
8 Gebauer, U. Gerstmann, C. Gougoussis, A. Kokalj, M. Lazzeri, L. Martin-Samos, N.  
9 Marzari, F. Mauri, R. Mazzarello, S. Paolini, A. Pasquarello, L. Paulatto, C. Sbraccia, S.  
10 Scandolo, G. Sclauzero, A. P. Seitsonen, A. Smogunov, P. Umari and R. M.  
11 Wentzcovitch, QUANTUM ESPRESSO: A modular and open-source software project for  
12 quantum simulations of materials, *J. Phys. Condens. Matter*, 2009, **21**, 395502.  
13  
14 28 D. Vanderbilt, Soft self-consistent pseudopotentials in a generalized eigenvalue  
15 formalism, *Phys. Rev. B*, 1990, **41**, 7892–7895.  
16  
17 29 K. F. Garrity, J. W. Bennett, K. M. Rabe and D. Vanderbilt, Pseudopotentials for high-  
18 throughput DFT calculations, *Comput. Mater. Sci.*, 2014, **81**, 446–452.  
19  
20 30 J. P. Perdew, K. Burke and M. Ernzerhof, Generalized gradient approximation made  
21 simple, *Phys. Rev. Lett.*, 1996, **77**, 3865–3868.  
22  
23 31 J. W. Bennett, D. T. Jones, R. J. Hamers and S. E. Mason, First-principles and  
24 thermodynamics study of compositionally tuned complex metal oxides: cation release  
25 from the (001) surface of Mn-rich lithium nickel manganese cobalt oxide, *Inorg. Chem.*,  
26 2018, **57**, 13300–13311.  
27  
28 32 X. Rong, J. Parolin and A. M. Kolpak, A fundamental relationship between reaction  
29 mechanism and stability in metal oxide catalysts for oxygen evolution, *ACS Catal.*, 2016,  
30 **6**, 1153–1158.  
31  
32 33 B. Delley, From molecules to solids with the DMol<sup>3</sup> approach, *J. Chem. Phys.*, 2000, **113**,  
33 7756–7764.  
34  
35 34 B. Delley, An all-electron numerical method for solving the local density functional for  
36 polyatomic molecules, *J. Chem. Phys.*, 1990, **92**, 508–517.

1  
2  
3 35 C. Lee, W. Yang and R. G. Parr, Development of the Colle-Salvetti correlation-energy  
4 formula into a functional of the electron density, *Phys. Rev. B*, 1988, **37**, 785–789.  
5  
6 36 C. A. Cohn, C. E. Pedigo, S. N. Hylton, S. R. Simon and M. A. A. Schoonen, Evaluating  
7 the use of 3'-(*p*-Aminophenyl) fluorescein for determining the formation of highly reactive  
8 oxygen species in particle suspensions, *Geochem. Trans.*, 2009, **10**, doi: 10.1186/1467-  
9 4866-10-8.  
10  
11 37 C. A. Cohn, S. R. Simon and M. A. A. Schoonen, Comparison of fluorescence-based  
12 techniques for the quantification of particle-induced hydroxyl radicals, *Part. Fibre Toxicol.*,  
13 2008, **5**, doi: 10.1186/1743-8977-5-2.  
14  
15 38 M. N. Hang, I. L. Gunsolus, H. Wayland, E. S. Melby, A. C. Mensch, K. R. Hurley, J. A.  
16 Pedersen, C. L. Haynes and R. J. Hamers, Impact of nanoscale lithium nickel  
17 manganese cobalt oxide (NMC) on the bacterium *Shewanella oneidensis* MR-1, *Chem.*  
18 *Mater.*, 2016, **28**, 1092–1100.  
19  
20 39 A. M. Schrand, J. J. Schlager, L. Dai and S. M. Hussain, Preparation of cells for  
21 assessing ultrastructural localization of nanoparticles with transmission electron  
22 microscopy, *Nat. Protoc.*, 2010, **5**, 744–757.  
23  
24 40 I. L. Gunsolus, M. N. Hang, N. V. Hudson-Smith, J. T. Buchman, J. W. Bennett, D.  
25 Conroy, S. E. Mason, R. J. Hamers and C. L. Haynes, Influence of nickel manganese  
26 cobalt oxide nanoparticle composition on toxicity toward *Shewanella oneidensis* MR-1:  
27 redesigning for reduced biological impact, *Environ. Sci. Nano*, 2017, **4**, 636–646.  
28  
29 41 P. Hovington, V. Timoshevskii, S. Burgess, H. Demers, P. Statham, R. Gauvin and K.  
30 Zaghib, Can we detect Li K X-ray in lithium compounds using energy dispersive  
31 spectroscopy?, *Scanning*, 2016, **38**, 571–578.  
32  
33 42 L. Li, J. Lu, Y. Ren, X. X. Zhang, R. J. Chen, F. Wu and K. Amine, Ascorbic-acid-assisted  
34 recovery of cobalt and lithium from spent Li-ion batteries, *J. Power Sources*, 2012, **218**,  
35 21–27.  
36  
37  
38  
39  
40  
41  
42  
43  
44  
45  
46  
47  
48  
49  
50  
51  
52  
53  
54  
55  
56  
57  
58  
59  
60

1  
2  
3 43 L. Li, J. Ge, R. Chen, F. Wu, S. Chen and X. Zhang, Environmental friendly leaching  
4 reagent for cobalt and lithium recovery from spent lithium-ion batteries, *Waste Manag.*,  
5 2010, **30**, 2615–2621.  
6  
7 44 E. Billy, M. Joulié, R. Laucournet, A. Boulineau, E. De Vito and D. Meyer, Dissolution  
8 mechanisms of  $\text{LiNi}_{1/3}\text{Mn}_{1/3}\text{Co}_{1/3}\text{O}_2$  positive electrode material from lithium-ion batteries in  
9 acid solution, *ACS Appl. Mater. Interfaces*, 2018, **10**, 16424–16435.  
10  
11 45 L. Macomber and R. P. Hausinger, Mechanisms of nickel toxicity in microorganisms,  
12 *Metalomics*, 2011, **3**, 1153–1162.  
13  
14 46 F. Barras and M. Fontecave, Cobalt stress in *Escherichia coli* and *Salmonella enterica*:  
15 molecular bases for toxicity and resistance, *Metalomics*, 2011, **3**, 1130–1134.  
16  
17 47 H. Sies, Strategies of antioxidant defense, *Eur. J. Biochem.*, 1993, **215**, 213–219.  
18  
19 48 A. C. Mensch, R. T. Hernandez, J. E. Kuether, M. D. Torelli, Z. V. Feng, R. J. Hamers  
20 and J. A. Pedersen, Natural organic matter concentration impacts the interaction of  
21 functionalized diamond nanoparticles with model and actual bacterial membranes,  
22 *Environ. Sci. Technol.*, 2017, **51**, 11075–11084.  
23  
24 49 Y. Tu, M. Lv, P. Xiu, T. Huynh, M. Zhang, M. Castelli, L. Zengrong, Q. Huang, C. Fan, H.  
25 Fang and R. Zhou, Destructive extraction of phospholipids from *Escherichia coli*  
26 membranes by graphene nanosheets, *Nat. Nanotechnol.*, 2013, **8**, 594–601.  
27  
28 50 X. Xing, W. Ma, X. Zhao, J. Wang, L. Yao, X. Jiang and Z. Wu, Interaction between  
29 surface charge-modified gold nanoparticles and phospholipid membranes, *Langmuir*,  
30 2018, **34**, 12583–12589.  
31  
32 51 S. Hussain, S. Garantziotis, F. Rodrigues-Lima, J.-M. Dupret, A. Baeza-Squiban and S.  
33 Boland, Intracellular signal modulation by nanomaterials, *Adv. Exp. Med. Biol.*, 2014, **811**,  
34 111–134.  
35  
36 52 O. Bondarenko, A. Ivask, A. Käkinen, I. Kurvet and A. Kahru, Particle-cell contact  
37 enhances antibacterial activity of silver nanoparticles, *PLoS One*, 2013, **8**, e64060.  
38  
39  
40  
41  
42  
43  
44  
45  
46  
47  
48  
49  
50  
51  
52  
53  
54  
55  
56  
57  
58  
59  
60

1  
2  
3 53 N. Von Moos and V. I. Slaveykova, Oxidative stress induced by inorganic nanoparticles in  
4 bacteria and aquatic microalgae - state of the art and knowledge gaps, *Nanotoxicology*,  
5 2014, **8**, 605–630.

6  
7 54 A. Okamoto, M. Yamamuro and N. Tatarazako, Acute toxicity of 50 metals to *Daphnia*  
8 *magna*, *J. Appl. Toxicol.*, 2015, **35**, 824–830.

9  
10 55 J. Bozich, M. Hang, R. Hamers and R. Klaper, Core chemistry influences the toxicity of  
11 multicomponent metal oxide nanomaterials, lithium nickel manganese cobalt oxide, and  
12 lithium cobalt oxide to *Daphnia magna*, *Environ. Toxicol. Chem.*, 2017, **36**, 2493–2502.

13  
14 56 J. A. Imlay, The molecular mechanisms and physiological consequences of oxidative  
15 stress: lessons from a model bacterium, *Nat. Rev. Microbiol.*, 2013, **11**, 443–454.

16  
17 57 Y. Jiang, Y. Dong, Q. Luo, N. Li, G. Wu and H. Gao, Protection from oxidative stress  
18 relies mainly on derepression of OxyR-dependent KatB and Dps in *Shewanella*  
19 *oneidensis*, *J. Bacteriol.*, 2014, **196**, 445–458.

20  
21 58 B.-T. Lee and J. F. Ranville, The effect of hardness on the stability of citrate-stabilized  
22 gold nanoparticles and their uptake by *Daphnia magna*, *J. Hazard. Mater.*, 2012, **213**,  
23 434–439.

24  
25 59 J. Towns, T. Cockerill, M. Dahan, I. Foster, K. Gaither, A. Grimshaw, V. Hazlewood, S.  
26 Lathrop, D. Lifka, G. D. Peterson, R. Roskies, J. R. Scott and N. Wilkins-Diehr, XSEDE:  
27 accelerating scientific discovery, *Comput. Sci. Eng.*, 2014, **16**, 62–74.

28  
29  
30  
31  
32  
33  
34  
35  
36  
37  
38  
39  
40  
41  
42  
43  
44  
45  
46  
47  
48  
49  
50  
51  
52  
53  
54  
55  
56  
57  
58  
59  
60

1  
2  
3 9. TOC Image  
4  
5  
6  
7  
8  
9  
10  
11  
12  
13  
14  
15  
16  
17  
18  
19  
20  
21  
22  
23  
24  
25  
26  
27  
28  
29  
30  
31  
32  
33  
34  
35  
36  
37  
38  
39  
40  
41  
42  
43  
44  
45  
46  
47  
48  
49  
50  
51  
52  
53  
54  
55  
56  
57  
58  
59  
60